Engineering Geology 264 (2020) 105333

Contents lists available at ScienceDirect

Engineering Geology

journal homepage: www.elsevier.com/locate/enggeo

Insights into bedrock paleomorphology and linear dynamic soil properties of the Cassino intermontane basin (Central Italy)

Michele Saroli[a,b], Matteo Albano[b,*], Giuseppe Modoni[a], Marco Moro[b], Giuliano Milana[b], Rose-Line Spacagna[a], Emanuela Falcucci[b], Stefano Gori[b], Gabriele Scarascia Mugnozza[c]

[a] Dipartimento di Ingegneria Civile e Meccanica, Università degli Studi di Cassino e del Lazio meridionale, via G. di Biasio 43, 03043 Cassino, Italy
[b] Istituto Nazionale di Geofisica e Vulcanologia, via di Vigna Murata 605, 00143 Roma, Italy
[c] Department of Earth Sciences and CERI Research Center on Geological Risks - Sapienza University of Rome, P. le Aldo Moro 5, 00185 Roma, Italy

ARTICLE INFO

Keywords:
Cassino basin
Seismic microzonation
Faults
Microtremor measurements
Geostatistics
Resonant frequency

ABSTRACT

Seismic amplifications are dictated by the depth of the bedrock and the stratigraphy and dynamic properties of the soil deposits. Quantifying these properties, together with their uncertainty, is a necessary task to perform a reliable assessment of the seismic risk at an urban scale. In this paper, a multidisciplinary analysis is presented, where information of different nature is combined. Borehole logs, geophysical, geological and geotechnical surveys are interpreted with the aid of analytical, numerical and geostatistical techniques to characterise the complex shape of the bedrock and the linear dynamic properties of the sedimentary deposits filling the Cassino basin, a Quaternary intermontane basin located in central Italy. The regional and local seismic hazard is firstly identified with geological surveys that reveal an active seismogenic fault capable of producing earthquakes with estimated magnitudes up to 6.7–6.8. Boreholes reaching depths variable up to a maximum of 180 m and microtremor measurements, revealing the sharp impedance contrast at the transition between the sedimentary/arenaceous bedrock and the soft Quaternary infilling, are combined to identify the depth of the bedrock and the linear dynamic properties of soil deposits. These are one of the key factors governing the propagation to the ground level of seismic waves, and their assessment represents the first step for the seismic hazard characterisation of the plain.

1. Introduction

Central Italy is one of the most seismically active areas in the Mediterranean region, as highlighted by the presence of several active faults and the occurrence of strong earthquakes in the past (Rovida et al., 2016; DISS Working Group, 2018). Faults have also played a primary role in shaping the landscapes of the Apennines mountain chain. In particular, the present active extensional tectonics favoured the development of several intermontane basins, bounded by seismogenic normal faults and filled by soft sedimentary soils.

Thanks to their favourable topographic and environmental conditions, these basins have promoted the development of ancient settlements in the past and dense urbanisation in recent times. The closeness of these developments to active, seismogenic faults is the basis of the high exposure to seismic hazard and risk for many urban settlements, civil infrastructures, industrial centres, and cultural heritage sites. Indeed, most of the recent earthquakes in central Italy caused severe damages and life loss in intermontane settlements (Bernard and Zollo, 1989; Amato et al., 1998; Galli et al., 2012, 2017).

Seismic risk is defined as the potential of negative consequences of hazardous events that may occur in a specific area and a period (Allin Cornell, 1968). It is given by the probabilistic convolution of three main components: seismic hazard, vulnerability and exposure. Seismic hazard assessment is a crucial factor and requires a thorough understanding of the seismic behaviour of active normal faults, both in time and space, and an in-depth investigation of the local geological and geotechnical features that impact on the modification of seismic ground motion and their local amplification (Bard and Bouchon, 1980; Şafak, 2001). In Italy, many studies have been performed both at regional and local scale to understand the seismic hazard of intermontane basins by means of in-situ investigations and numerical simulations (D'Amico et al., 2008; Cara et al., 2011; Del Monaco et al., 2013; Pagliaroli et al., 2015; Paolucci et al., 2016; Civico et al., 2017; Aucelli et al., 2018; Boncio et al., 2018; Milana et al., 2019). However, there are some areas where the local seismic hazard is still unknown.

Thanks to its geological and hydrogeological conditions, the Cassino

* Corresponding author.
E-mail address: matteo.albano@ingv.it (M. Albano).

https://doi.org/10.1016/j.enggeo.2019.105333
Received 17 May 2019; Received in revised form 27 September 2019; Accepted 10 October 2019
Available online 21 October 2019

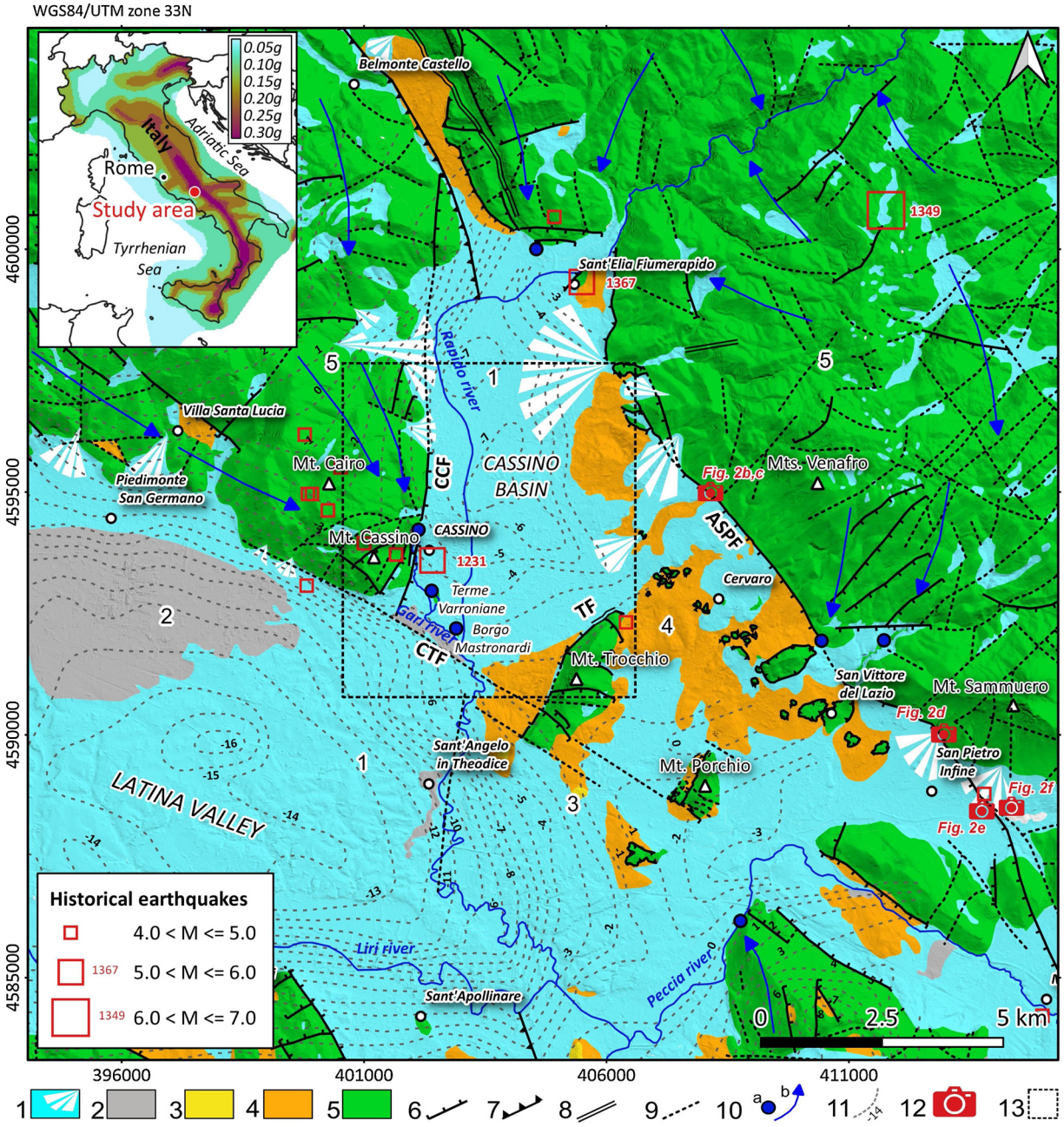

Fig. 1. Geological and hydrogeological map of the end sector of the Latina Valley, highlighting the main features of the fault system at the surface and the outcropping pre-Quaternary and Quaternary deposits, modified from Saroli et al. (2014). The inset shows the Italian seismic hazard map, with peak ground accelerations (g) that have a 10% chance of being exceeded in 50 years (Meletti and Montaldo, 2007). Key to the legend: 1) Recent and old debris, debris fans, eluvial, colluvial and lacustrine soils, interspersed with volcanic products (middle Pleistocene - Holocene). 2) Travertine (Middle Pleistocene - Upper Pleistocene). 3) Gravels and sands (Messinian - Lower Pliocene). 4) Sandstones and grey clays (flysch) (Upper Tortonian). 5) Limestones and dolostones with emipelagic marls (Lias - Lower Tortonian). 6) Normal faults. 7) Thrusts. 8) Strike-slip faults. 9) Inferred/buried faults. 10) Springs (a) and groundwater flux (b). 11) Isolines of the residual Bouguer anomaly (mGal) from Amadei et al. (1978). 12) Location of the pictures in Fig. 2. 13) Detail of the study area in Fig. 3. The historical earthquakes with magnitude M > 4 are taken from the parametric catalogue of Italian earthquakes (Rovida et al., 2016), the red number identifies the year of the event.

basin, located in central Italy, represents a remarkable example. The basin owes its name to the namesake town, an example of middle size Italian urban settlements, occupying the south-western part of the basin. Existing since the Roman age, Cassino has distinctive socio-economical, historical, environmental, geological, and hydrogeological features (Saroli et al., 2014, 2019). During the Second World War, the city was destroyed. Since then, the town was rebuilt, and the population underwent rapid growth, from about twenty to forty thousand people in less than 20 years. Over this period, the urban area considerably expanded over the alluvial plain at the foot of the Montecassino hill (Fig. 1) and several strategic infrastructures were built. Nowadays, the town hosts a middle-size University, critical civil infrastructures like the Campania aqueduct that provides water to more than 3 million people, the Busso-Paliano gas line and several significant industrial activities.

Historical and instrumental seismological data show that the Cassino basin has been affected by strong earthquakes in the past, with macroseismic intensities reaching grade 9 (Rovida et al., 2016). The probabilistic seismic hazard in this area, calculated from historical earthquakes, is among the highest in Italy (Meletti and Montaldo, 2007). The peak ground acceleration (PGA) at the bedrock, estimated

for 10% exceedance probability in 50 years, ranges between 0.20 and 0.25 g. (inset in Fig. 1) These values do not account for possible additional amplification caused by soft sedimentary deposits present in the area and by critical topographic conditions, given by the 3D geometry of the area. The few studies so far conducted focus on the geological, hydrogeological and environmental conditions of the basin. Based on the literature, in-situ, and remote sensing data, they provide just a preliminary outline on the subsurface basin geometry (Amadei et al., 1978; Polcari et al., 2014; Saroli et al., 2014, 2019; Albano et al., 2015). However, a more complete and detailed understanding of the mechanical characteristics of the subsoil, aimed at estimating the impact on the seismic ground motion and on the local amplifications, has not been undertaken. Quantifying the geometrical and mechanical characteristics of the soil deposit is crucial to develop scenario-based seismic hazard analysis, since wave reverberation and local ground-motion amplification could be triggered by sharp impedance contrasts at the interface between different formations, by the geometric complexity of the buried bedrock and, more generally, by the mechanical properties of the sedimentary deposit (Bard, 1985; Kramer, 1996; Bielak et al., 1999).

The goal of the present study is to provide an in-depth insight into the bedrock morphology, the stratigraphic conditions and the linear dynamic soil properties of the sedimentary infilling of the Cassino basin. To this aim, a multidisciplinary analysis is conducted combining borehole logs, geophysical measurements, and geological-geotechnical surveys to derive a preliminary dynamic model of the subsoil to be implemented in advanced microzonation studies of the area.

2. Geological, hydrogeological and seismological layouts of the Cassino basin

The Cassino area falls in a Plio-Pleistocene intermontane basin, located at the south-eastern edge of the Latina Valley, a broad and narrow depression with a northwest-southeast trend, developed since the Neogene along with the Apennines thrust and fold orogenic belt (Fig. 1). The basin has a northeast-southwest striking graben structure, with the deepest part of the depocenter located toward the north. This kind of structural setting is the result of the superposition of the Plio-Quaternary extensional tectonic phase on the fold-and-thrust structural edifice inherited from the previous contractional tectonic phase. Normal faults dissect the whole area, displacing the transpressive and compressive structures (Saroli et al., 2014). The main tectonic features of the region are the Atina-San Pietro Infine fault to the northeast (ASPF in Fig. 1) (Bosi, 1995; Roberts et al., 2002; Saroli and Moro, 2012), the Caira–Cassino fault to the west (CCF), and the Trocchio fault (TF) to the east. Those segments define the horst-and-graben structure of the basin, with the outcropping limestone platforms of *Terme Varroniane* and *Borgo Mastronardi* representing two intermediate horsts of this system (Fig. 1). Such an arrangement is confirmed by geological and hydrogeological evidence (Boni et al., 1986; Saroli et al., 2019). Moving to the south, the Cassino-Trocchio fault (CTF) dissects the Cassino plain with a deep disarticulation of the carbonate substratum. In this scenario, the thickness of the continental Plio-Quaternary cover varies from few tens of meters, close to the carbonate ridges, to several hundred meters in the northeastern part of the plain (Boni et al., 1982; Saroli et al., 2014). Bouguer gravity anomalies measured by Amadei et al. (1978) identify gradients with negative residuals up to -7 mGal to the northern part of the basin (Fig. 1).

The typical lithostratigraphic sequence of the Meso-Cenozoic bedrock starts with dolostones and limestones approximately 2000 m thick, pertaining to the Latium-Abruzzi carbonate platform, followed by ramp limestones and emipelagic marls, which widely outcrop over the study area (n°5 in Fig. 1). Tortonian post-collisional arenaceous and clayey deposits of epi-continental and continental origin cover the carbonate platform sequence (n°4 in Fig. 1), followed by Messinian piggy-back sequences formed during the compressive tectonics (n° 3 in Fig. 1) (Cipollari and Cosentino, 1995, 1999; Centamore et al., 2007; Pasquali et al., 2007).

Plio-Pleistocene continental lithologies deposited after the onset of extensional tectonics and the formation of the horst-and-graben system of the Latina Valley, close the sequence. The lowermost portion of the continental sequence is represented by gravel, sands and puddingstones (n°3 in Fig. 1), resulting by the progressive erosion of the Miocene ramp facies. These sedimentary units are followed upward by the volcanic products of the nearby Roccamonfina volcanic edifice. These volcanic deposits dammed the Latina Valley, changing the general environmental conditions from coastal to lacustrine, thus giving origin to the Lirino lake (Devoto, 1965) and the consequent deposition of lacustrine sediments made of sandy silts, with thin levels of raven ashes and volcanic products, interbedded. Travertine deposits and marsh silt mark the complete filling of the basin, on the top of the lacustrine series (n° 2 in Fig. 1). Travertine deposits outcrop to the south of the Cassino town (Fig. 1). This lithology ranges from spongy and vacuolar to loose and lithified sand, with an average thickness of approximately 15–18 m. The Cassino travertines close the lacustrine cycle and are related to the activity of the threshold of the Gari springs (Boni et al., 1986). The last volcanic events occurred in a continental-fluvial environment and originated the interfingering of volcanic sands and detrital layers. Late Pleistocene-Holocene fluvial environment (Rapido, Liri and Gari River) incised the lacustrine sequence and deposited 5–15 m of alluvial clayey silt, sand and gravel (n° 1 in Fig. 1). Nearby the calcareous bedrock, colluvial soils and alluvial fans can hide the relationship between the bedrock and Quaternary deposits.

The hydrogeological setting of the area is controlled by the carbonate karst aquifer of the Simbruini Ernici – Mt. Cairo hydrostructure, with high-discharge basal springs located at the most topographically depressed aquifer boundaries of the Cassino town, and the *Terme Varroniane – Borgo Mastronardi* carbonate outcrops (Fig. 1) (Saroli et al., 2019). These springs, with a mean discharge up to 13-18 m^3/s (Boni, 2003), are among the largest spring groups in Italy thus far. About 4 m^3/s are taken to provide water to the city of Naples and its hinterland.

The hydrostructure is dissected by a continuous network of fractures, increasing the effective porosity and contributing to the high permeability and discharge rates. The other hydrogeological complexes (n°4, 3, 2, and 1 in Fig. 1) are heterogeneous, with impermeable horizons made of clay or clayey silts, alternating with medium-to-high permeability layers of coarse sands and gravels, allowing the development of local perched aquifers, often confined. The local aquifers are steadily fed by lateral contact with the carbonate karst aquifer. The depth of the mean water table in the Cassino basin is almost stationary and located a few meters below the ground level (Saroli et al., 2019).

The seismicity of the area is related to the activity of normal fault systems, northwest-southeast oriented (e.g., Upper Sangro fault system, Mount Rotella–Cinquemiglia–Aremogna Plains fault system and northern Matese faults) (Galli and Naso, 2009), spreading over the central-southern Apennine chain, and characterised by medium-to-large magnitude seismic events. Moderate earthquakes ($M_w < 6$) have struck the Cassino basin in past centuries, with intensities ranging between 6–8 Mercalli-Cancani-Sieberg (MCS) (Rovida et al., 2016), whose location is still uncertain. Among the regional strongest earthquakes, the January 1915, Avezzano earthquake ($M_w = 7.0$) nucleated more than 60 km north of the Cassino basin and caused extensive damage in the area, with a maximum estimated macroseismic intensity of 7 MCS. The largest earthquake of the area is the catastrophic event of September 1349 (Fig. 1) ($M_w \cong 6.8$) (actually, the event had been a seismic sequence), with devastating effects in the Cassino town, and an estimated macroseismic intensity up to 9 MCS (Rovida et al., 2016). Historical chronicles reported that most of the destruction and collapses in Cassino happened in specific portions of the town, which notably are those portions built on the alluvial plain. These findings highlight a possible amplification of ground motion caused by local geological

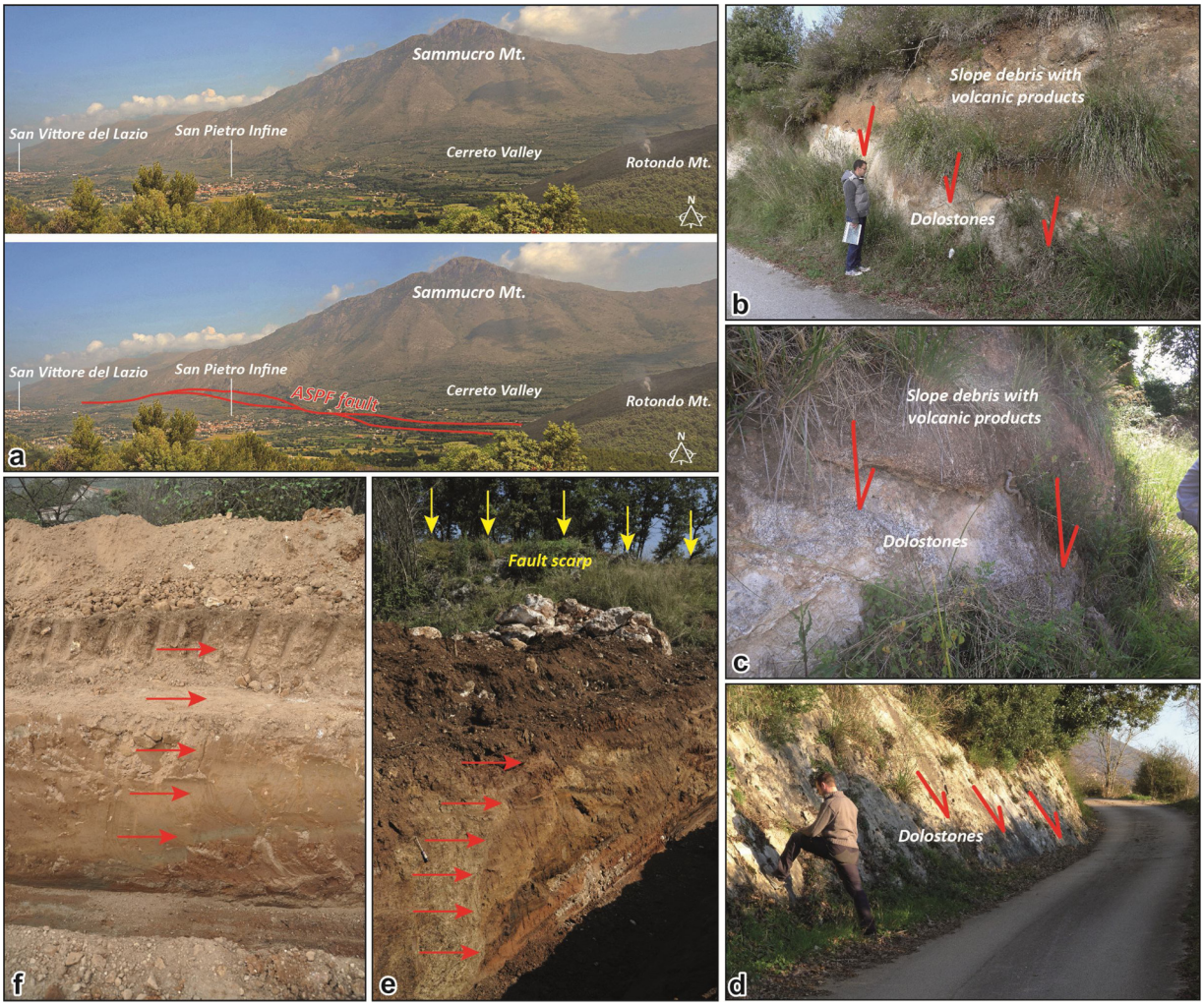

Fig. 2. Geological surveys along the ASPF fault. For the location of the pictures, see Fig. 1. a) Panoramic view of the ASPF fault (the red line). b) Slope debris with volcanic products in tectonic contact with the fault plane in dolostones. c) Detail of panel b. d) Dip-slip fault plane made of dolostones. e) and f) Evidence of ASPF faulting in upper Pleistocene-Holocene deposits.

conditions. The primary seismogenic source associated with this event is still uncertain, with some studies attributing it to the nearby Acquae-Iuliae fault (Galli and Naso, 2009), bounding to the east the nearby Venafro basin. Nonetheless, the ASPF segment (Fig. 1) represents another structural feature of the area, which affected the Cassino basin itself, and which may have played and may still play an essential role in the seismotectonics of the area, as a local source of potentially destructive earthquakes. This fault extends over about 25–30 km, passing through the towns of Belmonte Castello, Sant'Elia Fiumerapido, Cervaro, San Vittore del Lazio and San Pietro Infine (Figs. 1 and 2a). Previous seismological studies defined this tectonic feature as active (Galadini et al., 2000, 2012; Roberts and Michetti, 2004), as it shows evidence of activity since Lias (Cavinato and Sirna, 1988) to the Quaternary, and with an estimated slip rate of approximately 0.3–0.5 mm/yr (Barchi et al., 2000). Recent surveys (Saroli and Moro, 2012) highlighted that the fault dissected and displaced recent deposits and landforms (flights of fluvial terraces), dated approximately at the Late Pleistocene – Holocene (Fig. 2b, c and d). Those findings suggest the activity of the fault and its capability to generate large magnitude earthquakes, of the order of about M ≅ 6.7–6.8, according to the Wells and Coppersmith (1994) regression. Evidence of very recent activity has also been found within two trenches dug across the fault for the installation of public facilities (for the location see Fig. 1). The trenches (Fig. 2e, f) showed the presence of displaced Holocene deposits containing pottery shards likely of Roman age. Apart from the 1349 seismic sequence, and the 1654 earthquake which, however, affected the Sora basin area, located some tens kilometres north of the Cassino area, the latter has not been the focus of large magnitude earthquakes over the past millennium (Rovida et al., 2016). Given the evidence of very recent activity, the ASPF might represent a critical active, dormant fault, that is, an important seismic gap.

3. Data and methodology

A systematic investigation has been performed to characterise the seismic response of the subsoil, quantifying the properties of the cover units, the presence of impedance contrasts, and the depth of the seismic bedrock. The procedure is articulated in the following steps:

i Collection, classification and interpretation of a large number of geological, geotechnical and geophysical data;
ii Execution over the study area of an extensive campaign of measurement with single microtremor station and spatial mapping of the resonant frequencies;
iii Calculation of a first-order mean Vs profile of the Quaternary sedimentary soils;
iv Estimation of the depth of the seismic bedrock.

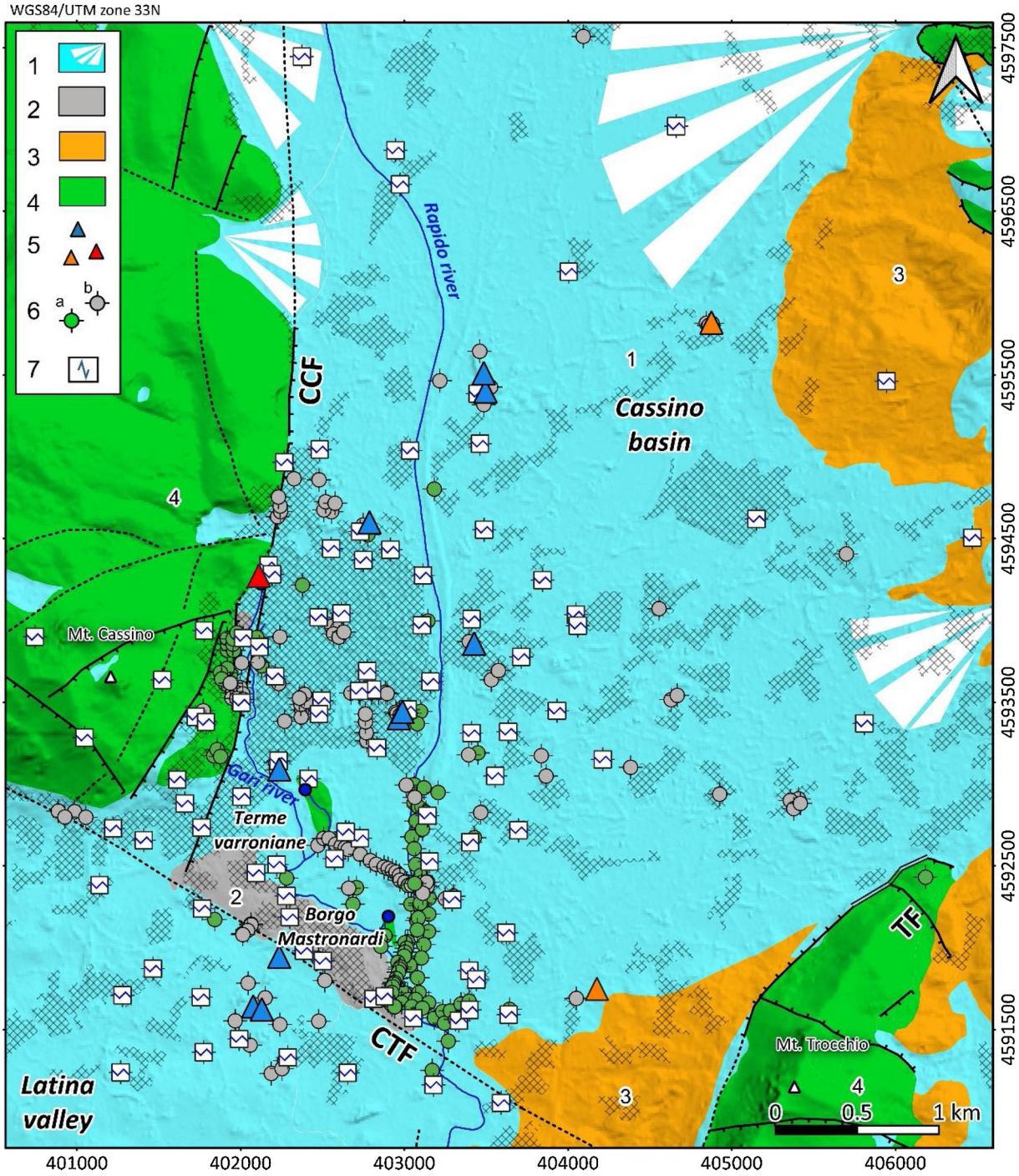

Fig. 3. Detail of the inset in Fig. 1 showing the location of the available data. Key to the legend: 1) Recent and old debris, debris fans, eluvial, colluvial and lacustrine soils, interspersed with volcanic products (middle Pleistocene - Holocene). 2) Travertine (Middle Pleistocene - Upper Pleistocene). 3) Sandstones and grey clays (flysch) (Upper Tortonian). 4) Limestones and dolostones with emipelagic marls (Lias - Lower Tortonian). 5) Available MASW and Down-Hole measurements (the different colours correspond to the Vs profiles in Fig. 7c. 6) Boreholes reaching (a) and do not reaching (b) the pre-quaternary sedimentary (n°4) and terrigenous (n°3) basement. 7) Microtremor measurements. For the other symbols, please refer to the legend in Fig. 1.

3.1. Data collection

The collected data consist of stratigraphy from boreholes, geophysical investigations, and laboratory geotechnical investigations (Fig. 3). In detail, 83 wells over a total number of 220 (green circles in Fig. 3) were drilled down to the pre-Quaternary arenaceous and sedimentary bedrock up to 350 m depth for oil research and groundwater exploitation (Novarese, 1926; Beneo, 1942; Celico and Stanganelli, 1978). They show the morphology of the bedrock and the thickness of Quaternary deposits (Saroli et al., 2014, 2019). The remaining 137 shallow boreholes (grey circles in Fig. 3), drilled in the Quaternary layer only, provide information about the geotechnical properties of the shallow deposits.

Available geophysical data consists of 16 shear-wave (Vs) velocity profiles from MASW and Down-Hole measurements up to 35 m depth (coloured triangles in Fig. 3). Such data were exploited for the estimation of a mean Vs-depth relationship for the shallow soil layers and to identify shallow impedance contrasts eventually.

3.2. Execution and processing of microtremor surveys

Single-station microtremor surveys were performed during two campaigns in the period 2008–2009 and 2011, respectively (Fig. 3). In the first campaign (2008–2009) microtremors were recorded at 73 sites, mainly located in the urban area of the Cassino town. Measurements were carried out using a three-component LE3D seismometer by Lennartz Electronics GmbH with 5 s eigenperiod (http://www.lennartz-electronic.de/index.php/seismometers-en/le-3d-5s), coupled with a REFTEK 130 datalogger (http://www.trimble.com/Infrastructure/Trimble-REF-TEK-130S-01.aspx) and set to a sampling frequency of 125 Hz. The recording length was approximately 30 min, recommended for spectral analysis at least down to 0.5 Hz (SESAME, 2004; Molnar et al., 2018). In the second campaign (2011), further 27 measurements were performed with three SS-1 seismometers by Kinemetrics Inc. (http://www.rsuw.daleh.id.au/SS-1_Ranger_seismometer.pdf) with 1-second eigenperiod and coupled with a K2 datalogger with a sampling frequency of 200 Hz. The recording length was approximately 20 min.

Microtremor acquisitions in the urban environment of the Cassino town presented significant challenges since transient signals, such as road traffic and machinery, impacted on the measurement quality. To improve the signal-to-noise ratio, recordings were performed at a distance of more than 10 m from infrastructures and at different times during the day and night (Molnar et al., 2018). Recordings at a site were repeated in case of inconsistency with the results of neighbouring measurements.

Microtremor recordings of ambient noise were exploited for the evaluation of the site period (or fundamental frequency) of unconsolidated sediments over high-velocity bedrock according to the noise horizontal-to-vertical spectral ratio method (hereinafter NHVSR) (Nakamura, 1989). NHVSR method is a widely used reconnaissance tool for seismic microzonation and earthquake site characterisation. Specifically, this method is exploited for the retrieval of site resonant period or fundamental frequency, and inverted for shear-wave velocity depth profiles (Parolai et al., 2002; Gallipoli et al., 2004; Gosar and Lenart, 2010; Gosar et al., 2010; Del Monaco et al., 2013; Gorstein and Ezersky, 2015; Borges et al., 2016; Tarabusi and Caputo, 2016; Civico et al., 2017; Rosa-Cintas et al., 2017; Salameh et al., 2017; Iannucci et al., 2018; Molnar et al., 2018). The technique consists of spitting the three components (two horizontal and one vertical) of a microtremor measurement into several time windows of equal or varying length. Windows affected by strong noise transients are manually or automatically removed. Smoothed Fourier spectra are then computed for each of the three components, and the ratio between the horizontal spectrum, given by the mean of the two horizontal components, and the vertical spectrum is performed for each time window. Finally, the horizontal-to-vertical spectral ratios of each time window are averaged to calculate the mean NHVSR curve (Molnar et al., 2018). Empirical evidence shows that the NHVSR curve shows an amplitude peak at a frequency corresponding to the resonant frequency of the subsoil over the investigated site. On the contrary, the peak amplitude overestimates the seismic amplification in case of earthquakes; thus, it cannot be used to estimate earthquake site amplification (Bard, 1999; SESAME, 2004).

The NHVSR curve for each measurement is estimated with the Geopsy code (www.geopsy.org). Recorded time series were visually inspected to identify possible erroneous measurements and strong transient noise. All the three spatial components (north-south, east-west and up-down) of the recorded time history were then divided into non-overlapping windows of 40 s. Amplitude spectra were computed in the frequency range 0.25–20 Hz with the fast Fourier transform and using a triangular window with 5% tapering. The Fourier spectra were smoothed with the Konno–Ohmachi function (Konno and Ohmachi, 1988) with a bandwidth coefficient b = 40. The ratio between the horizontal and vertical components was then computed for each window as the geometric average of the two horizontal spectral components divided by the vertical spectrum. A directional NHVSR analysis was also performed at 10° angular steps to identify the possible directions of the noise sources. The latter was analysed by estimating the NHVSR curves derived by projecting the ground motion along with different horizontal directions.

3.2.1. Spatial analysis of soil resonant frequencies

The spatial relationship between the NHVSR-derived resonant frequencies (hereinafter RF) has been investigated using a geostatistical approach. Geostatistical methods, i.e., Kriging interpolation techniques (Krige, 1951, 1966; Matheron, 1963; Isaaks and Srivastava, 1989), comprise a range of least-squares methods to provide the best linear unbiased predictions, best in the sense of minimum variance (Oliver and Webster, 2014). Such methods can integrate auxiliary information by employing appropriate interpolation algorithms such as co-kriging (CK) and kriging with external drift (KD) (Hudson and Wackernagel, 1994; Knapmeyer-Endrun et al., 2016; Trevisani et al., 2017), and have been widely used to map spatial data (Modoni et al., 2013; Tarabusi and Caputo, 2016; Trevisani et al., 2017; Trevisani and Boaga, 2018).

The geostatistical analysis of the experimental RF has been performed according to the following steps (Oliver and Webster, 2014):

i Preliminary exploratory spatial analysis of the experimental RFs for the identification of possible trends, distortions, and outliers;
ii Calculation of the experimental variogram and identification of possible anisotropies;
iii Fitting of the experimental variogram with a theoretical model. For the available dataset, we used a spherical plus nugget model of Eq. (1) (Oliver and Webster, 2014):

$$\gamma(h) = \begin{cases} c_0 + c\left\{\dfrac{3h}{2r} - \dfrac{1}{2}\left(\dfrac{h}{r}\right)^3\right\} & 0 < h \le r \\ c_0 + c & h > r \\ 0 & h = 0 \end{cases} \quad (1)$$

where h is the lag distance, r is the range, c_0 is the nugget and $c_0 + c$ is the sill;

i Interpolation of the experimental data by ordinary kriging and estimation of the associated variance (or standard deviation);
ii Evaluation of the performance of the interpolation with a leave-one-out cross-validation analysis (CV). The procedure consists of sequentially removing a point from the dataset and predicting that value with the variogram model. The difference between the prediction and the original value is then calculated for each point of the dataset.

The errors are assessed in terms of their statistical and spatial distribution (Trevisani et al., 2017) and with diagnostic measures such as the mean error (ME), the mean absolute error (MAE), the root mean squared error (RMSE), and the Mean Squared Deviation Ratio (MSDR) of the residuals to the prediction errors.

The exploratory analysis, the spatial mapping, the cross-validation, and the presentation of the results for the available dataset have been performed using the geostatistical package Gstat (Pebesma, 2004), accessible through the open-source R code (R Core Team, 2018), together with the open-source GIS environment QGIS (QGIS Development Team, 2018).

3.3. Average shear-wave (Vs) profile

The present study aims at providing a first-order seismic characterisation of the basin by exploiting the available set of Vs profiles, the RF estimated from the NHVSR analysis, and the available bedrock depth measured at boreholes. Therefore, an average velocity-depth function for the Quaternary soils has been defined according to the following equation (Ibs-von Seht and Wohlenberg, 1999; D'Amico et al.,

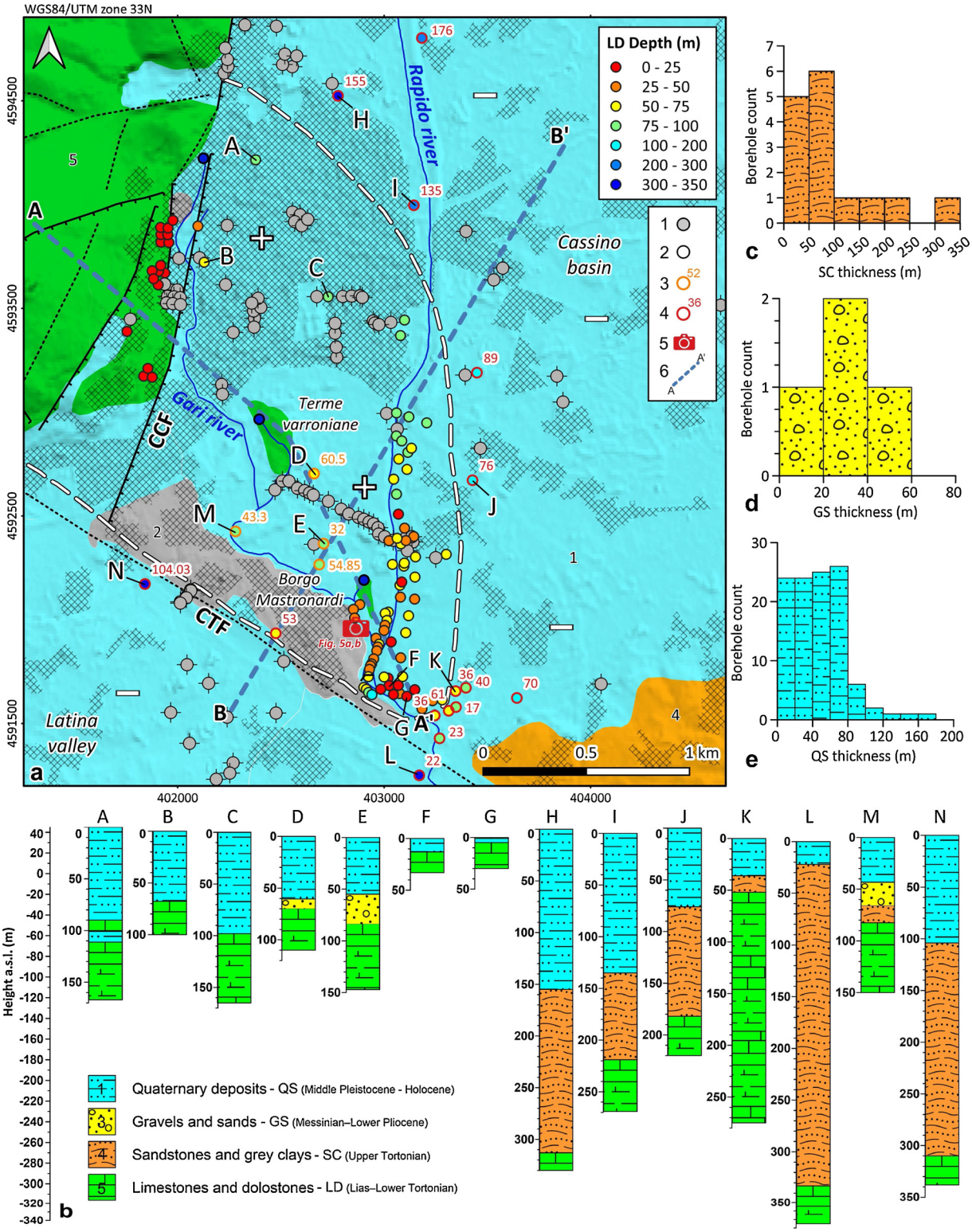

Fig. 4. Results from the analysis of the available boreholes on the Cassino basin. a) Borehole location and classification. Key to the legend: 1) Boreholes intercepting the QS layer only; 2) Boreholes intercepting the QS and the LD layers (the fill colour indicates the depth of the LD layer according to the colour palette in panel a); 3) Boreholes intercepting the QS, GS and LD layers, with the orange number identifying the roof depth of GS layer; 4) Boreholes intercepting the QS, SC and LD layers, with the red number identifying the roof depth of the SC layer. 5) Location of the pictures in Fig. 6. 6) Trace of the cross-sections in Fig. 5. The dashed blue lines define the trace of the cross-sections in Fig. 5. For the other symbols refer to Fig. 1 and Fig. 3. b) Stratigraphy of selected boreholes in panel a. c) d) e) Distribution of the investigated thickness for the SC (c), GS (d) and QS (e) layers.

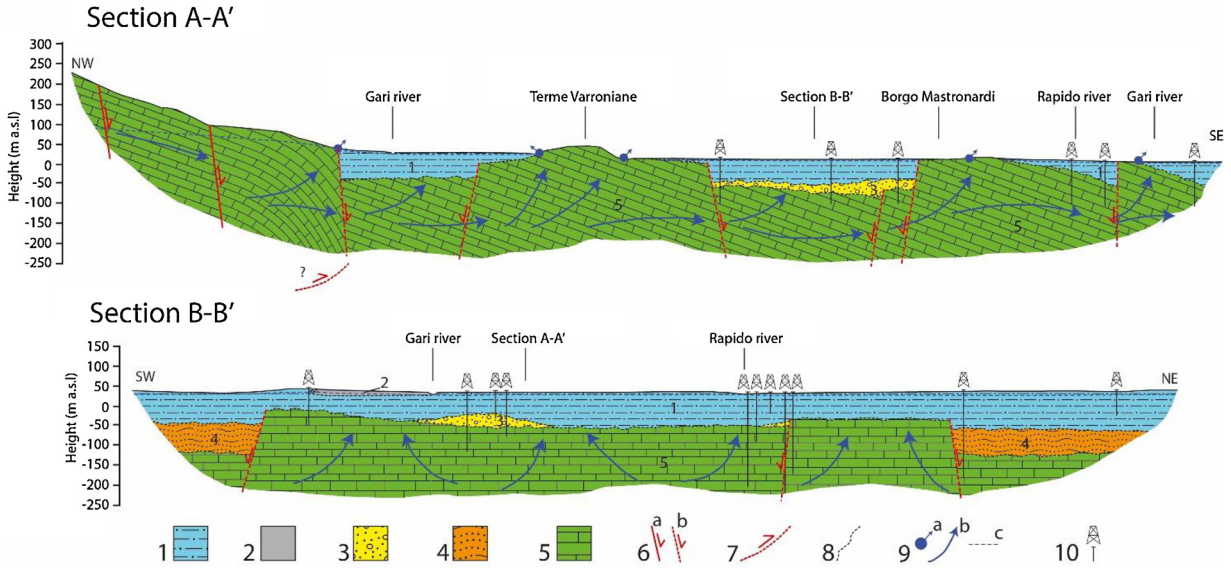

Fig. 5. Geological and hydrogeological cross-sections along the Cassino basin, modified from Saroli et al. (2014, 2019). For the location, see Fig. 4. Key to the legend: 1) Quaternary soils (QS). 2) Travertine (TR). 3) Gravels and sands (GS). 4) Sandstones and grey clays (flysch) (SC). 5) Limestones and dolostones (LD). 6) Normal faults: a) certain; b) inferred. 7) Inferred thrust. 8) Inferred lithological boundary. 9) (a) Springs, (b) groundwater flux, and (c) piezometric level. 10) Boreholes.

2008):

$$V_s(z) = V_{s0}(1 + {}^{z}/_{z_0})^x \quad (2)$$

where z is the depth below the ground, $z_0 = 1$ m, V_{s0} is the shear wave velocity at the surface, and x is an exponential term defining the depth-dependence of the shear-wave velocity (Ibs-von Seht and Wohlenberg, 1999; D'Amico et al., 2008; Gosar and Lenart, 2010).

The coefficients of Eq. (2), i.e., V_{s0} and x, are calibrated in two ways:

i by best fitting the available experimental Vs profiles;
ii by exploiting the available RF, estimated from the NHVSR analysis, and the bedrock depth measured from boreholes (H).

In the latter case, a simple monotonic relationship can be defined between H and RF, according to the following equation (D'Amico et al., 2008; Gosar and Lenart, 2010; Gosar et al., 2010; Del Monaco et al., 2013; Gorstein and Ezersky, 2015):

$$H \cong aRF^b \quad (3a)$$

In Eq. (3a), a and b are empirical coefficients, which are estimated by sampling the interpolated RF map in correspondence of the available boreholes reaching the seismic bedrock and by best fitting the RF-H data with the power-law regression curve of Eq. (3a).

A further simple relationship between H and RF can be expressed in terms of V_{s0} and an additional coefficient x according to the following equation (Ibs-von Seht and Wohlenberg, 1999):

$$H = \left[\frac{V_{s0}(1-x)}{4RF} + 1\right]^{1/(1-x)} - 1 \quad (3b)$$

The combination of Eqs. (3a) and (3b) allows estimating the V_{s0} and x coefficients of Eq. (2) from the a and b coefficients, according to the following equations:

$$a = \left[\frac{V_{s0}(1-x)}{4}\right]^{1/(1-x)} \quad (4a)$$

$$b = -\frac{1}{1-x} \quad (4b)$$

Feasibility of such an approach requires that the sedimentary layer be spatially homogenous over the whole basin.

3.4. Thickness of the Quaternary layer

The depth of the seismic bedrock, i.e., the thickness H of the amplifying layer, can be estimated by Eq. (3b). Such an equation implies that the amplifying layer presents a Vs profile characterised by a single couple of coefficients V_{s0} and x, according to Eq. (2).

In case of the presence of two layers (layer 1 and layer 2) separating at a transition depth H^* and characterised by a different Vs profile, the coefficients of Eq. (3b), i.e., V_{s0} and x, particularize in $V_{s0,1}$ - x_1 and $V_{s0,2}$ – x_2 for layers 1 and 2, respectively. In such a case, Eq. (3b) becomes (D'Amico et al., 2008):

$$H = \begin{cases} \left[\frac{V_{s0,1}(1-x_1)}{4RF} + 1\right]^{1/(1-x_1)} - 1 & \text{for } RF > RF_t \text{ (Layer 1)} \\ \left[\frac{V_{s0,2}(1-x_2)}{4RF} + C\right]^{1/(1-x_2)} - 1 & \text{for } RF \le RF_t \text{ (Layer 2)} \end{cases} \quad (5)$$

In Eq. (5), RF_t is a threshold frequency corresponding to the transition depth (H^*) between the first and second layer, given by the following equation (D'Amico et al., 2008):

$$RF_t = \frac{V_{s0,1}(1-x_1)}{4[(1+H^*)^{1-x_1} - 1]} \quad (6a)$$

and C is a coefficient calculated by the following relation (D'Amico et al., 2008):

$$C = (1+H^*)^{1-x_2} - \frac{V_{s0,2}(1-x_2)}{V_{s0,1}(1-x_1)}[(1+H^*)^{1-x_1} - 1] \quad (6b)$$

4. Results

4.1. Morphology, geology and geotechnical properties of the Cassino basin

About 90% of the available boreholes provided the complete log of the geological column, thus allowing to study both the morphology of the Cassino basin and the relationship between the observed lithologies. The analysis of the deep boreholes allowed a first reconstruction of the carbonate basement and the relationship between carbonates (LD; n°5 in Fig. 1), sandstones and grey clays (SC; n°4 in Fig. 1), gravels and sands (GS; n°3 in Fig. 1), and Quaternary deposits (QS; n°1 in Fig. 1).

The LD basement is hugely uneven (coloured circles showing the LD

Fig. 6. a) Surveyed springs along the Rapido River b) Detail of the panel a. For the location of the pictures, see Fig. 4a.

depth in Fig. 4a). The investigated top-depths vary from a few meters close to the *Mt. Cassino*, *Terme Varroniane* and *Borgo Mastronardi* outcrops, to more than 300 m towards the centre of the Cassino Basin to the northeast and the Latina Valley to the southwest. The depth variation is abrupt, indicating the possible presence of several buried faults (Fig. 5). Moving from northwest to southeast, the CCF fault downthrows the LD bedrock up to 100 m, as testified by the boreholes A to C in Fig. 4b and Section A-A' in Fig. 5. Buried faults also dissect the two outcropping horsts of *Terme Varrionane* and *Borgo Mastronardi*, which bound a graben where the LD reaches 90-meter depth (boreholes D and E in Fig. 4b and Section A-A' in Fig. 5). A third horst is located to the southeast, at the confluence of the Gari and Rapido rivers (drillings F and G in Fig. 4b). The presence of subcropping LD is also confirmed by in-situ surveys that testified the presence of previously unmapped springs with a significant groundwater discharge (Fig. 6) (Saroli et al., 2014, 2019).

To the northeast, the LD roof-depth downthrows from approximately 100 m (boreholes A to C) to more than 300 m (boreholes H to J in Fig. 4b and Section B-B' in Fig. 5) because of the joint action of buried fault segments below the Quaternary sediments and the ASPF fault to the northwest (Fig. 1) (Saroli et al., 2014, 2019). To the southwest of the *Terme Varroniane* and *Borgo Mastronardi* outcrops, the intense activity of the CTF fault is testified by boreholes L and N. Indeed, LD bedrock sinks from approximately 80 m (borehole M) to more than 300 m (boreholes L and N) in less than 250-meter distance (Section B-B' in Fig. 5). Therefore, the area approximately bounded by the dashed white line in Fig. 4a results on a structural high (plus symbol) concerning the rest of the basin.

Outside the dashed white line (minus symbol) the available boreholes intercept the SC lithology (circles with a red outline in Fig. 4a). SC widely outcrops to the northeast and southeast of the Cassino plain (Fig. 1) and shows an investigated thickness ranging from few meters up to 350 m (Fig. 4c and boreholes H to N in Fig. 4b). Discontinuous banks of GS layer up to 40 m thick (Fig. 4d) occur in the graben between the *Terme Varroniane* and *Borgo Mastronardi* horsts (circles with an orange outline in Fig. 4a; boreholes D, E and M in Fig. 4b; Section A-A' in Fig. 5) (Saroli et al., 2014). Finally, the QS layer shows an investigated thickness ranging from a few meters up to 180 m (Fig. 4e). The QS lays on the LD basement over the area inside the white dashed line in Fig. 4a (boreholes A to G in Fig. 4b), and on the SC layer outside, with the occasional presence of the GS layer (boreholes D, E and M in Fig. 4b).

The shallow boreholes allowed to investigate the physical properties of the soils filling the Cassino basin up to 30-meter depth. Grain size distributions performed on samples at different depths (Fig. 7a) show significant fractions of silt and clay with a limited amount of sands and gravels (less than 30%). However, lenses of coarse-grained deposits (up to 50%) with a scarce fraction of fines are often observed throughout the investigated depth. The natural unit weight of soils, measured in laboratory tests, is constant with depth, with a mean value of approximately 18 kN/m^3 (Fig. 7b).

The available shear-wave velocity (Vs) profiles from MASW and Down-Hole measurements (Fig. 7c) performed on the QS layer (light blue profiles in Fig. 7c) show a general increase of Vs with depth with an estimated mean $Vs_{,30}$ of approximately 320–350 m/s (soil type C according to the Eurocode 8) and without sharp velocity contrasts. A few measurements performed close to the boundary between QS and the LD and SC lithologies (the red and orange triangles in Fig. 3, respectively) identified a bright velocity contrast at depth. In particular, the two dotted orange profiles in Fig. 7c (for the location see Fig. 3) identify a velocity contrast up to 650–700 m/s at approximately 10–13 meter depth, associated with the shallow transition between the QS and SC layer. Instead, the dashed red profile shows a sharp velocity contrast with Vs up to 1200 m/s at approximately 8-meter depth, associated with the contact between the QS and LD layer.

4.2. NHVSR results and spatial mapping

The NHVSR curves computed for each available measurement are shown in Fig. 8 (for the location of each measurement, see Fig. A.1 in Appendix A). In Appendix A, the computed H/V spectral ratio curve is superimposed to the directional plot in Fig. A.2 for each measurement, while the mean spectral amplitudes of the three components of the noise are shown in Fig. A.3.

Before interpreting the obtained H/V peaks according to the subsoil dynamic properties, we checked the possible occurrence of measurement issues and anomalous peaks in the NHVSR curve. Some measurements were disregarded because of recording issues in one of the three components of the noise (e.g., R9, RC13, and RC23 in Fig. A.3). Some other measurements present sharp peaks on all the three single-component spectra at frequencies of approximately 1.5 Hz and 5 Hz (e.g., R7, R10, and R34 in Fig. A.3). Those peaks show a strong directionality (Fig. A.2) and, in some cases, mask the resonant frequency of the site on the NHVSR curve, thus making the measurement useless. The nature of those peaks is clearly of industrial origin since some measurements, repeated at night in the same locations, did not show anomalous frequency peaks, thus allowing to define the resonant frequency at the site (Fig. A.4). The remaining measurements were grouped into three classes, according to the outcropping lithology where each measurement was performed, i.e., the LD layer, the SC

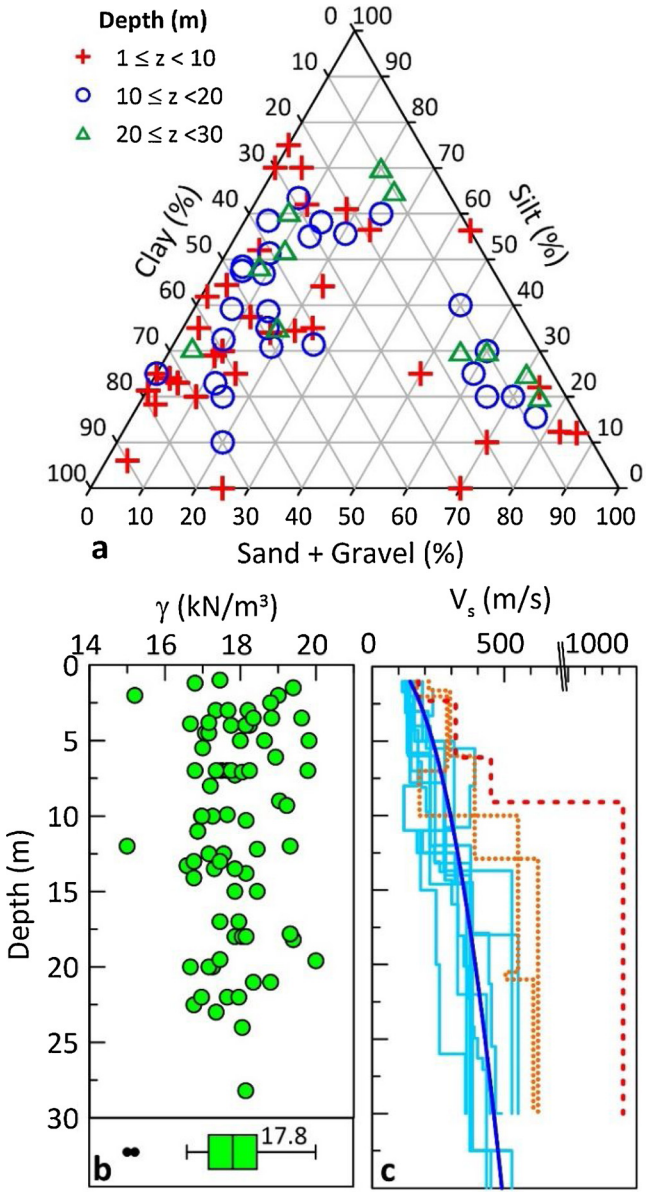

Fig. 7. a) Soil grain size percentages from available grain size distributions at different depths. b) Distribution of natural unit weight with depth from laboratory tests. c) Shear-wave profiles from available MASW and Down-Hole measurements. The colour of each profile corresponds to the coloured triangles located in Fig. 3.

layer, and the QS layer.

Measurements performed over the LD layer (Fig. 8a) do not show any significant frequency peaks. Some broad high-frequency peaks could be associated with the degree of fractures opening or with geomorphic and structural complexities of the ridges (Pagliaroli et al., 2015). Measurements performed on the SC layer (Fig. 8b) are also flat. Therefore, the absence of a sharp impedance contrast at the contact between SC and LD layers, together with the rather high stiffness of the LD and SC lithologies (i.e., Vs ≥ 700 m/s according to Vs measurements; Fig. 7c) implies that both lithologies can be classified as seismic bedrock, according to the Italian regulations (MIT, 2018).

Measurements over the QS soils were grouped according to the shortest distance between the measurement point and the LD and SC outcrops (hereinafter DOB) (Fig. 8c–i). NHVSR curves show significant frequency peaks over the range 0.6–3.4 Hz. For small DOB (DOB < 200 m), peak frequencies are heterogeneous and difficult to interpret because of deviations from the assumption of 1D stratigraphy caused by geometrical and lithological heterogeneities in the subsoil. For higher DOB values (DOB > 200 m), i.e., moving towards the centre of the basin, amplitude peaks shift towards lower frequencies, according to the increase of the bedrock depth (Fig. 4a). Those frequency peaks are generally bright and often sharp, thus were interpreted as the resonant frequencies (RF) of the site. For each H/V curve, we assessed the presence of one or more resonant peaks fulfilling the criteria of reliability and clarity defined by the SESAME working group (SESAME, 2004). Measurements not fulfilling the SESAME criteria were disregarded. However, some of them were considered as relevant RF since they were consistent with those at closest locations. The spatial distribution of the RF values (Fig. 8j) shows a strong correlation with the general morphology of the basin. RFs in the range 2–3.4 Hz result near the *Terme Varroniane* and *Borgo Mastronardi* carbonate outcrops and the Mt. Cassino hills, thus testifying the presence of a shallow impedance contrast. RFs gradually decrease going away from the rocky outcrops to the northwest and southeast, with the lowest values of 0.6-0.8 Hz reached towards the centre of the Cassino basin.

The spatial mapping of the computed RF over the QS soils has been performed employing a geostatistical analysis. To improve the geostatistical interpolation, we worked with resonance periods (RP = 1/RF) instead of RF, as suggested by Trevisani et al. (2017). We also introduced the dependency between the RFs (or RPs) and the DOB observed in Fig. 8 by using the Kriging with external drift (KD) interpolation technique (Oliver and Webster, 2014), with the DOB assumed as an auxiliary variable in the interpolation procedure. Consequently, the explorative spatial analysis, the estimation of the experimental variogram, and the fitting with a theoretical variogram model have been conducted on data residuals respect to a trend map that defines the general RP trend in the Cassino basin (Fig. B.2a in Appendix B). The experimental variogram has been analysed using both variogram cloud, variogram map, directional and omnidirectional variograms, showing the absence of anisotropies, local outliers, or other patterns related to non-stationarity. The final isotropic experimental variogram has been fitted with the isotropic spherical plus nugget model of Eq. (1). Once defined the theoretical variogram of the RP residuals, we interpolated the RPs together with the trend map of Fig. B.2a using KD. Details about the exploratory spatial analysis, the variogram analysis, the geostatistical interpolation, and the cross-validation analysis of the KD interpolation are reported in Appendix B.

The obtained RP map is shown in Fig. 9a, while the standard deviation error (Std) of the predicted RP map is shown in Fig. 9b. The RP map is blanked on the areas where the prediction variance is larger than the third quantile of the variance distribution (i.e., 0.0263 s^2), corresponding to a maximum standard deviation of 0.162 s (Fig. 9b).

4.3. Estimation of the average Vs profile

The average V_S profile for the QS layer has been estimated using the available shallow Vs profiles, deep boreholes, and the results of microtremor surveys. At shallow depth, i.e., up to 30–35 meters, the mean Vs profile has been estimated by best fitting with Eq. (2) (blue curve in Fig. 7c) the available experimental Vs curves from MASW and Down-Hole surveys performed on the QS layer (light blue curves in Fig. 7c). The best-fit *Vo* and *x* coefficients are reported in Eq. (7) for Layer 1, while the corresponding mean Vs profile is the red curve in Fig. 10a (RMSE = 90, R^2 = 0.65).

At greater depth, we investigated the existence of an experimental relationship between the RF and the QS thickness (*H*). In detail, the interpolated RP map in Fig. 9a has been converted to RFs and sampled in correspondence of the deep boreholes crossing the QS layer (Fig. 3 and Fig. 4). RF values with a standard deviation higher than 0.2 Hz (Fig. 9b) were discarded. The comparison between RF and *H* from boreholes (Fig. 10b) shows that RF is inversely proportional to the QS thickness. The monotonic relationship between *H* and RF has been

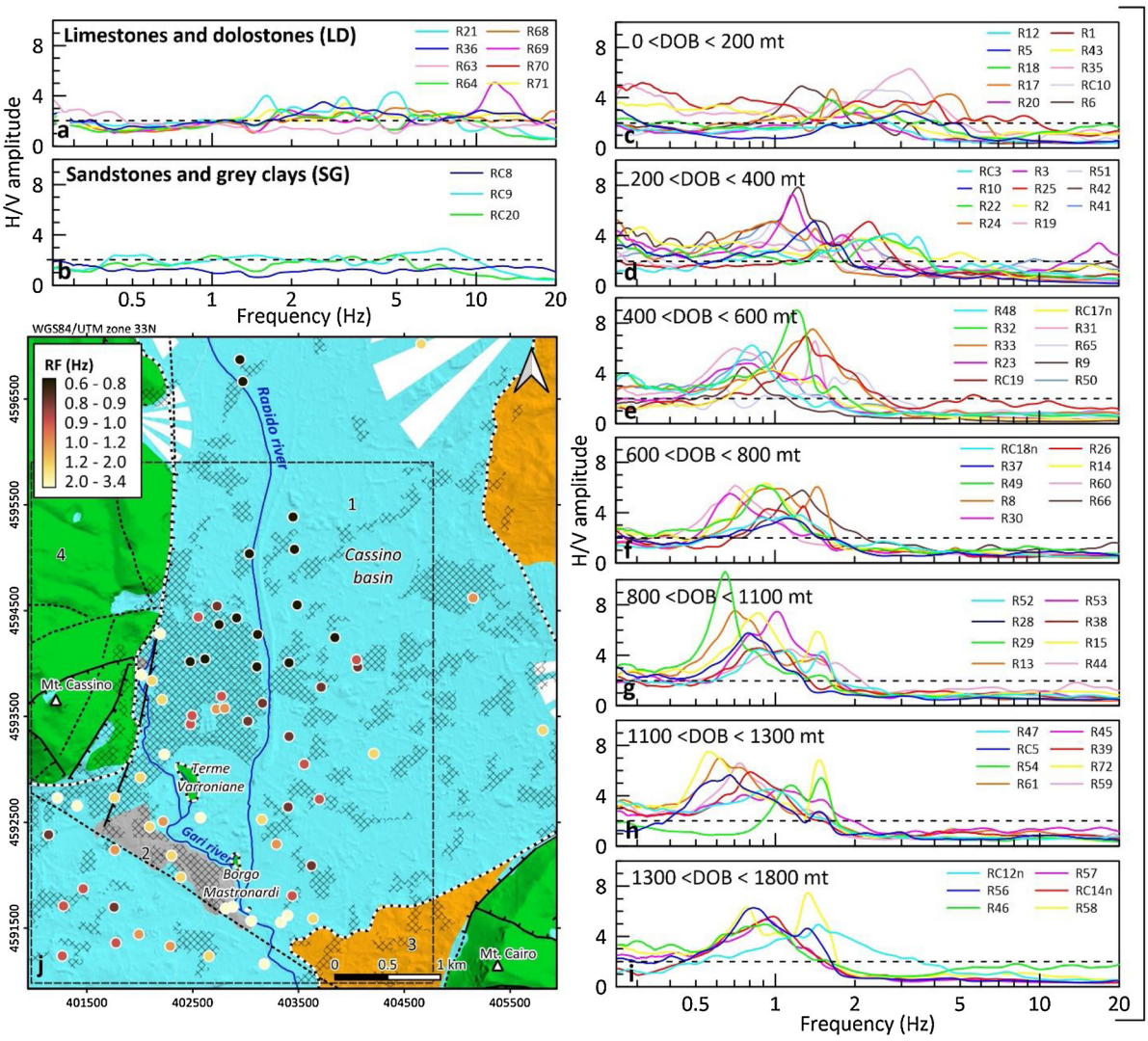

Fig. 8. Results of the NHVSR processing. a) H/V curves from microtremor measurements performed on the LD layer. b) H/V curves from microtremor measurements performed on the SC layer. c–i) H/V curves from microtremor measurements performed on QS layer, classified according to the DOB. j) Classed post map of RF values estimated for measurements performed on QS layer (classes according to quantile classification). The dashed black and white line identifies the boundary of the outcropping seismic bedrock. For the other symbols, please refer to Fig. 1.

estimated with Eq. (3a) (R^2 = 0.84, RMSE = 12.7), whose best-fit coefficients are a = 95.1 and b = -1.312, respectively. Then, a mean Vs profile has been computed with Eq. (2), where the V_0 and x coefficients (Layer 2 in Eq. (7)) are estimated from the experimental a and b coefficients from Eq. (4a) and (4b). The resulting Vs profile is shown as the green curve in Fig. 10a, and it is representative of QS thickness ranging approximately between 30 and 180 m (Fig. 10b).

The blue line in Fig. 10a represents the final average Vs profile for the QS layer. This profile accounts for the shallow (layer 1) and deep (layer 2) Vs trends. The two experimental profiles intersect at approximately H^* = 11 m; therefore, Eq. (2) for the blue Vs profile becomes (7):

$$V_s(z) = \begin{cases} 106.9\left(1 + {}^{z}/_{z_0}\right)^{0.426} & \text{for } z < 11\,m\ (Layer\ 1) \\ 169\left(1 + {}^{z}/_{z_0}\right)^{0.238} & \text{for } z \geq 11\,m\ (Layer\ 2) \end{cases} \quad (7)$$

The average Vs profile of Eq. (7) has been exploited for the calculation of the theoretical 1D transfer function (hereinafter TF) between the surface and the seismic bedrock at selected boreholes reaching the seismic bedrock and located at a distance lower than 50 m from the nearest microtremor measurement. The TF has been computed with the STRATA code (Kottke et al., 2013), which implements the Random Vibration Theory (RVT) approach, which does not require the application of time-domain input motions. The theoretical TF has been then compared with the experimental NHVSR curve for validation (Nguyen et al., 2004; Oubaiche et al., 2016).

The 1D column is made of a homogeneous linear-elastic material corresponding to the QS layer in Fig. 4b, resting on an elastic half-space representing the seismic bedrock, which corresponds, alternatively, to the SC and LD layers (Fig. 4b and Fig. 11). The 1D column presents a thickness equal to the measured QS thickness from boreholes, mean unit weight of 18 kN/m^3 (Fig. 7b), a viscous damping ratio of 5%, and a mean Vs profile given by Eq. (7) (blue curve in Fig. 10a). An average Vs = 1000 m/s has been assumed for the underlying half-space. The uncertainty in the definition of the shear wave profile with depth for the QS layer is introduced in the STRATA code by assuming a log-normal distribution for the mean Vs value at the mid-depth of the generic ith-layer (Toro, 1996; Toro et al., 1992), with a logarithmic standard deviation of 0.31 (the dashed blue curves in Fig. 10a). The dependency of stiffness and equivalent damping on shear strains is ignored since natural microtremors do not involve soil degradation and plasticization. Therefore, we are investigating the linear dynamic behaviour of soils only.

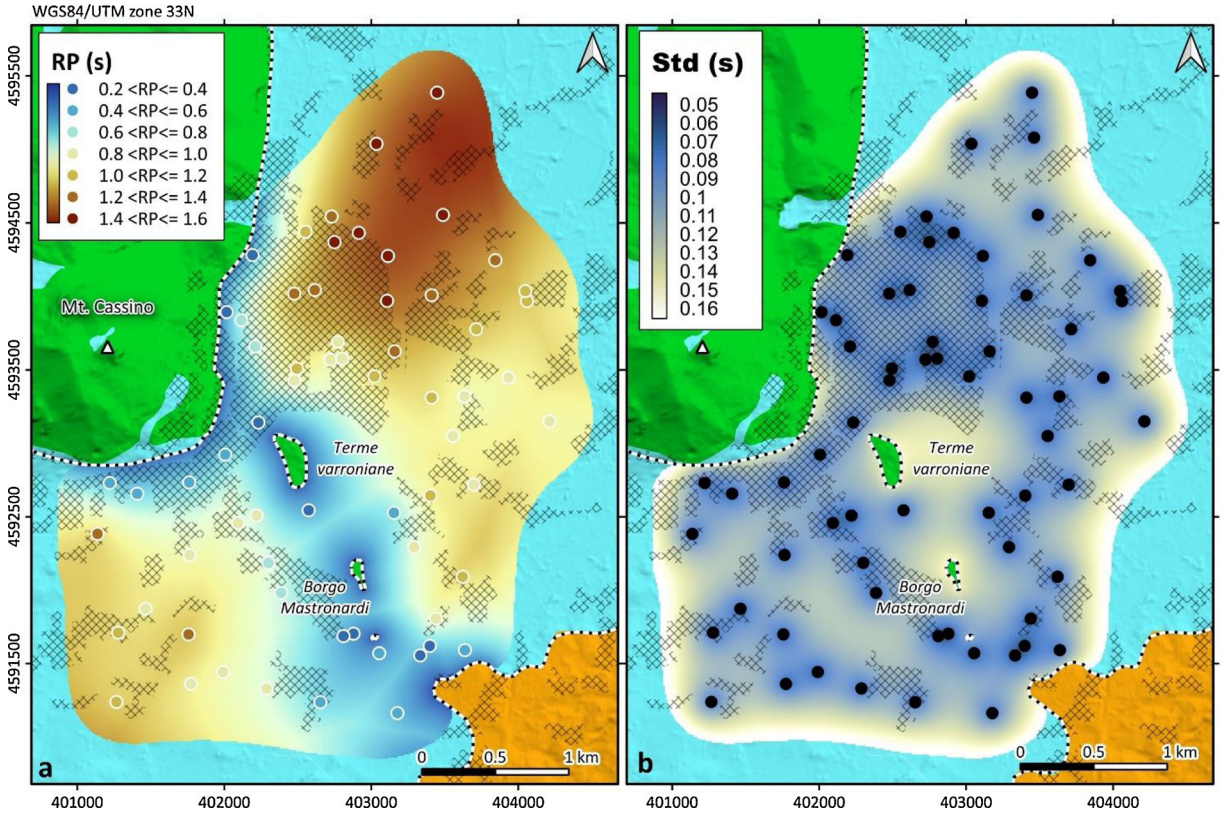

Fig. 9. Results of the geostatistical analysis performed on the RP values. a) Interpolated map of RP via block KD. The circles identify the measured RP from microtremors. b) KD prediction standard deviation map of RP. The black circles identify the location of microtremor measurements. The dashed black and white line identifies the boundary of the outcropping seismic bedrock.

The code automatically performs a Monte Carlo simulation, where the response of the system is computed for 200 realisations assuming different Vs profiles. The TFs from each realisation are then used to estimate the statistical properties of the system's response employing a mean TF curve and the associated standard deviation.

The analysis has been performed for six boreholes (Fig. 11), and the resulting mean TF (black curve), with its standard deviation (grey area), is compared with the experimental NHVSR curve (red curve). The general agreement between TF and NHVSR curves testifies the validity of the computed first-order Vs profile. Indeed, the first peak amplitude occurs at approximately the same frequency for both TF and NHVSR curves, corresponding to the first resonant frequency of the soil column.

4.4. Thickness of the QS layer

Finally, the QS thickness H (i.e., the depth of the seismic bedrock) has been estimated from the RP map of Fig. 9a, opportunely converted in RF, using Eq. (5) with $H^* = 11$ m and the V_{s0} and x coefficients reported in Eq. (7). The resulting thickness map (Fig. 12a) shows that H varies between few meters close to the seismic bedrock, i.e., the LD and SC outcrops (Vs ≥ 700 m/s), up to 120–180 meters towards the Latina Valley and the Cassino basin, respectively.

The accuracy of the QS thickness map has been evaluated by comparing the prediction map with the measured thickness at the available deep boreholes. The comparison between measured and predicted H values (Fig. 12b) has a RMSE of 15.5 m and a MAE of 12.3 m. The

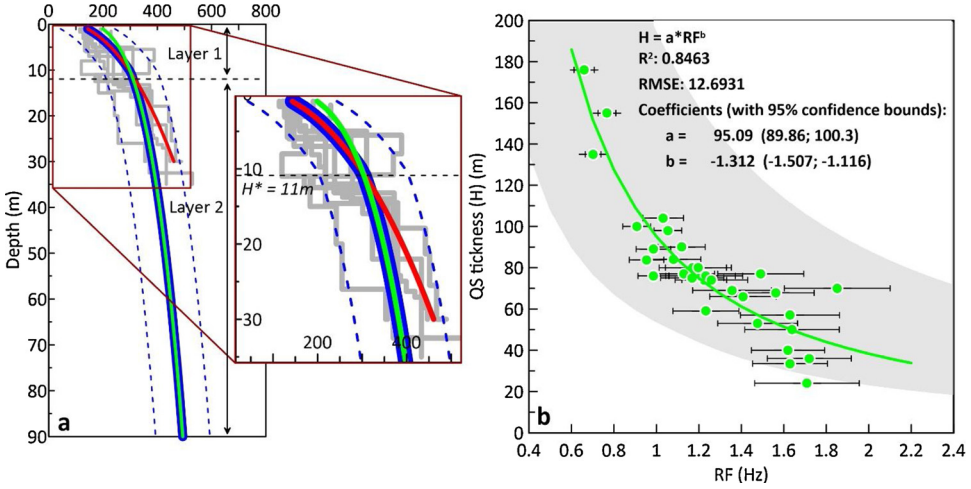

Fig. 10. Estimation of a mean shear wave velocity profile for the QS layer. (a) Mean Vs velocity profiles, according to Eq. (2): The red curve is computed from available MASW and DH profiles; the green curve is calculated from the experimental RF-H relationship in panel b. The blue curve is the profile adopted for the QS layer. (b) The empirical relationship between RF and QS thickness (H). The grey area includes the experimental *RF-H* relationships available from the literature (Ibs-von Seht and Wohlenberg, 1999; D'Amico et al., 2008; Gosar and Lenart, 2010; Del Monaco et al., 2013).

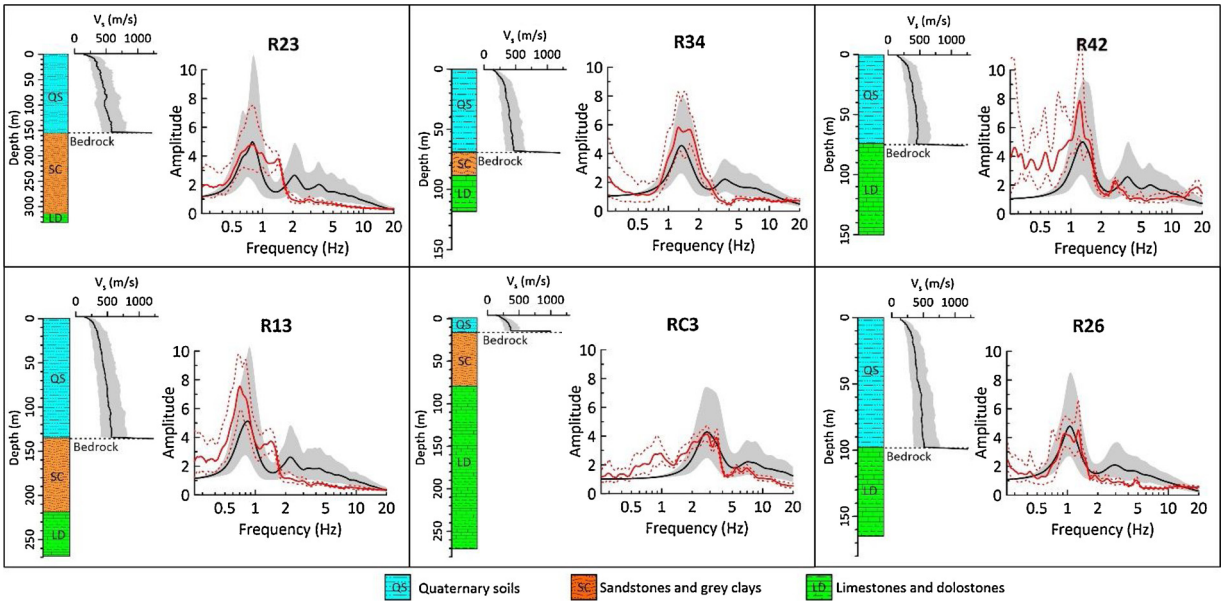

Fig. 11. Calculation of the elastic transfer function at six boreholes and comparison with the NHVSR curve from adjacent microtremor measurements. From left to right in each panel: Borehole stratigraphy, with the indication of the assumed seismic bedrock in the 1D simulations; Vs profile assumed for the QS layer; comparison between the theoretical TF (black line) and the experimental NHVSR curve (red line).

statistical distribution of the errors, i.e., the difference between the measured and predicted thickness at the same point, is positively skewed (Fig. 12c), meaning that the prediction map generally underestimates the observations. Overall, 50% of the absolute errors is less than 10 m, and 75% is less than 18 m (Fig. 12d). The mean relative percentage error, i.e., the error expressed as a percentage of the measured thickness, is approximately 25%, while half of the measurements show a relative error less than 20% (Fig. 12e). Finally, the spatial distribution of the relative errors (Fig. 12f) shows that the higher relative errors are associated to boreholes located close to the Mt. Cassino hills and the *Terme Varrioniane – Borgo Mastronardi* bedrock outcrops, where the bedrock shape is probably more complex.

5. Discussion

In this work, a thorough analysis of multidisciplinary data from borehole logs, new and available geophysical measurements, and geological-geotechnical surveys, unveils for the first time the features of the subsurface of the Cassino basin and the dynamic properties of the sedimentary infilling, thus allowing to speculate on the subsurface geometry and on the local ground-motion amplification phenomena. This study provides first insights about the factors affecting the regional and local seismic hazard of the area and allows for a first-order assessment of the resonant frequencies (or periods) and thickness of the quaternary infilling, as well as its average shear stiffness.

The Cassino basin presents several topographic highs, and it is dissected by faults (Fig. 1) that downthrow the pre-Quaternary sedimentary and terrigenous lithologies (LD and SC layers in Fig. 4) up to 350 m at depth. Among the main faults bounding the basin, new geological surveys testify the capability of the ASPF fault to the northeast to generate strong earthquakes up to M 6.7–6.8. Above the pre-Quaternary basement, the thickness of the QS infill is exceptionally uneven (Fig. 12a), being thinner close to the *Terme Varroniane* and *Borgo Mastronardi outcrops*, and gradually thickening up to 180 m towards the depocenters of the Cassino basin and the Latina valley.

Microtremor recordings identify sharp frequency peaks at measurements laying on the QS layer (Fig. 8), which are interpreted as the RF of the sedimentary infilling. RF is proportional to the thickness of the QS layer (*H*) (Fig. 10b), with low/high RF values corresponding to the thick/thin QS layer. RFs are associated with a sharp impedance contrast at the transition between the QS layer and the underlying layers (Fig. 4). Such impedance contrast is related to substantial variations in both density (Fig. 7b) and shear stiffness (Fig. 7c) between the QS layer and the underlying layers. Microtremor measurements performed on the LD and SC layers (Fig. 8a and b) do not show any significant resonant frequency peaks. Therefore, these findings suggest that the seismic bedrock resembles with the contact between the QS layer and, alternatively, the SC layer or the LD layer. The latter lithologies show a high shear stiffness, with Vs ≥ 700 m/s (Fig. 7c) and can be assumed as the seismic bedrock of the site, as also confirmed by 1D numerical simulations (Fig. 11).

The estimated mean Vs profile of the QS layer (Fig. 10a) shows two different trends. The shallow part has a steeper increase of Vs with depth respect to the deeper part. Moreover, the value of V_S at the surface (V_{s0}) for layer 1 (i.e., $V_{s0,1}$ = 106.9 m/s) is much lower than that resulting by extrapolating to the surface the Vs trend obtained for layer 2 (i.e., $V_{s0,2}$ = 169 m/s). This finding suggests that the two different Vs trends reflect different sedimentary environments. The shallower profile is associated with alluvial soils, while the deeper one to fluviolacustrine soils. The two profiles provide nearly the same V_S value at a depth of approximately 11 m, that is, at the depth where, on average, the transition between alluvial and fluviolacustrine environment occurs (Saroli et al., 2014). The lack of any significant jump of seismic impedance at this transition may explain the general lack of secondary NHVSR peaks generated from this interface (Fig. 8).

Regarding local seismic amplification, microtremor measurements performed on the QS layer (Fig. 8) show significant peak amplitudes. Most of the urban settlements lie on the QS layer, with thicknesses varying between 20 and 120 m (Fig. 12a) and resonant frequencies between 0.9–3 Hz (Fig. 8j and Fig. 9a). Those frequencies are typical of ordinary buildings in civil engineering design; therefore, possible resonance effects could be expected in case of earthquakes. Soil liquefaction is also likely, since the available grain size distributions identified several lenses of sandy to silty soils at shallow depth, lying below the mean groundwater level (Fig. 7a and cross-sections in Fig. 5).

The interpolated RP map of Fig. 9a and the RP trend map of Fig. B.2a provide further interesting features that are worthy of analysis. In particular, the RP residuals map, i.e., the difference between the RP

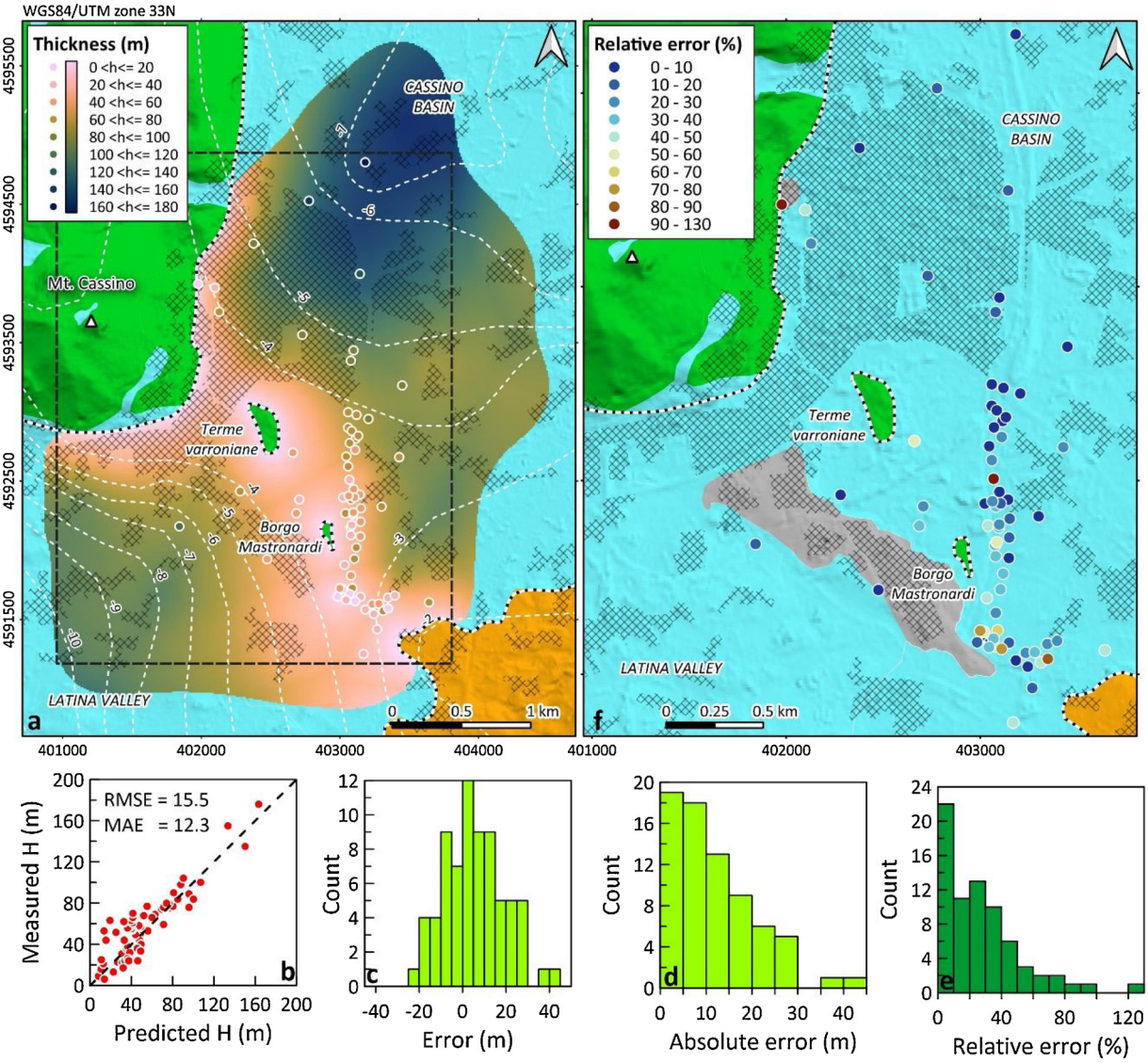

Fig. 12. Computation and performance of the QS thickness map (*H*). a) QS thickness map computed with Eq. (5) from the available RF map. The small circles indicate the QS thickness measured from boreholes. The dashed black and white line identifies the boundary of the outcropping bedrock (the LD and SC outcrops). The dashed white curves identify the isolines of the residual Bouguer anomaly (mGal) from Amadei et al. (1978) b) Scatter diagram of observed values of *H* plotted against values computed with Eq. (5). c) Histogram of the prediction errors. d) Histogram of absolute prediction errors. e) Histogram of relative prediction errors expressed as a percentage of the measured thickness measured at boreholes. f) Detail of panel a (the black dashed rectangle) showing the spatial distribution of the relative percentage error calculated at each available borehole reaching the seismic bedrock.

map and the trend map (Fig. A.5b), can be related to local variations of the bedrock depth and of the Vs of the sedimentary cover (Trevisani et al., 2017). Since the Vs profile for the QS layer is reasonably uniform (Fig. 7c), areas of negative RP residuals indicate a locally shallower bedrock than expected and vice-versa. Such a finding agrees with available boreholes (Fig. 4) that show a sudden increase of the bedrock depth to more than 150 m in the northern sector, while a gentler increase is observed southwestward. A further key feature of the RP residual map is the abrupt variation between positive and negative anomalies, highlighted by the white dashed lines in Fig. A.5. Those variations can be related to tectonically disturbed areas, located in correspondence to fault lines or morphological scarps characterising the bedrock surface. Indeed, the orientation of the identified discontinuities agrees with the prevalent northeast-southwest and northwest-southeast direction of the main normal faults that bound the Cassino basin (Fig. 1). In detail, discontinuities perfectly overlap with both CCF and CTF alignments and identify further buried segments bordering the *Terme Varrioniane* and *Borgo Mastronardi* outcrops, according to the cross-sections in Fig. 5. However, such discontinuities are not captured by the QS thickness map of Fig. 12a. Such an issue is associated to the spatial resolution of the microtremor data used for the calculation of the QS thickness, which allows depicting the first-order topographic features of the basement only. Local-scale heterogeneities and details related to buried faults and erosional or depositional features are not sufficiently sampled. The QS thickness map derived from the RP map is smooth and captures with discrete accuracy the general trend of the basement, but the comparison with the QS thickness measured from boreholes shows unavoidable errors, especially in areas close to the bedrock outcrops (Fig. 12f), where boreholes identify local heterogeneities (Figs. 4 and 5). Unfortunately, the strong spatial clusterization of the available boreholes (Fig. 3) and the absence of any spatial correlation between thickness data (not shown), did not allow the application of geostatistical techniques (i.e., Ordinary Kriging, co-Kriging or Kriging with external drift) for a direct estimation of the bedrock basement depth (or the QS thickness).

The available data do not allow to investigate the entire basin.

Indeed, the uneven distribution of the microtremor surveys, clustered in the nearby of the Cassino city centre, increases the uncertainty of the geostatistical interpolation and produces an unacceptable variance on areas where measurements are sparse. Moreover, the presence of spurious frequency peaks of industrial origin in the microtremor signals (Fig. A.3) and local deviations of the subsoil from the 1D hypothesis, causes noticeable uncertainties in the RF values of the QS layer, especially for measurements performed close to the bedrock outcrops (Figs. 8 and 10b).

A solution to these issues is to increase both the number of microtremor measurements and the recording time on specific areas characterised by strong topographic gradients and sparse surveys. Other types of geophysical surveys, e.g., gravimetric and shear-wave velocity measurements, could also be considered to improve the knowledge of the basin. To this purpose, the geostatistical analysis provided not just the interpolated RP map of the area (Fig. 9a), but also the associated uncertainty (Fig. 9b). This latter is fundamental to understand the accuracy of the interpolation, but also to identify areas that require further investigations because of high uncertainty in the estimation of RP. The RP map in Fig. 9a has a maximum standard deviation of 0.16 s, which has deemed acceptable for a first-order characterisation of the basin. Such a threshold is subjective and depends on the intended use of the interpolated map. It has been assumed acceptable for the first-order analysis deemed to this study, but it could be inappropriate for local-scale studies (Trevisani et al., 2017).

The available data allowed to investigate the linear dynamic properties of the Cassino subsoil only. Further surveys are required, together with numerical simulations, to investigate the nonlinear dynamic properties of the soils (e.g., resonant column tests or cyclic triaxial tests) and the seismic amplification in case of strong earthquakes.

Although the obtained results may not currently allow for a detailed description of the geometrical and dynamic features of the Cassino basin, the first-order results are robust. The experimental *RF-H* curve in Fig. 10b is typical of shallow-to-medium depth quaternary basins, and it is comparable with those obtained from other case studies (the grey area in Fig. 10b) (Gosar and Lenart, 2010; Del Monaco et al., 2013; Bignardi, 2017). The sharp impedance contrast identified by resonant frequency peaks in the NHVSR curves on the QS layer agrees with the historical evidence of massive damage for settlements located in the Cassino basin respect to those on the Montecassino hill during the 1349 earthquake (Galli and Naso, 2009). Finally, the estimated subsurface basin geometry (Fig. 12a) is consistent with the residual gravimetric anomaly map of Amadei et al. (1978) (Figs. 1 and 12a), produced independently in the same area. Indeed, the areas with maximum infill thickness (i.e., maximum bedrock depth) match well the negative Bouguer anomalies.

6. Conclusions

In this work, the joint analysis of multidisciplinary data from borehole logs, geophysical measurements, and geological-geotechnical surveys provides a first-order picture of the Cassino basin bedrock morphology and the dynamic properties of the sedimentary infilling. The results show that the regional and local seismic hazard of the investigated area is modulated by:

- The nearby Atina-San Pietro Infine (ASPF) fault, which is estimated to be capable of generating earthquakes with magnitudes up to 6.7–6.8;
- The complex shape of the buried seismic bedrock;
- The sharp impedance contrast between the seismic bedrock and the Quaternary infilling.

Those factors play a fundamental role in the generation and propagation of the seismic waves since local ground-motion amplification is primarily controlled by geometric complexities in the buried bedrock topography and sharp seismic velocity contrasts (Ewald et al., 2006; Vessia and Russo, 2013).

The results of this study can be considered as the first step toward a scenario-based seismic hazard analysis and the associated risk for infrastructures at a basin-wide scale of the Cassino plain. Since the available data allow to investigate the linear dynamic properties of the soils only, further investigations are required to assess their nonlinear dynamic behaviour.

As the input data are always to some extent uncertain, it is essential to have a sufficiently large number of measurements to improve the accuracy of the results. For this purpose, the geostatistical analysis of the NHVSR frequency peaks identified areas where further investigations are needed to improve the knowledge of the investigated area.

Data availability

The data used to support the findings of this study are available upon request to the corresponding author.

Declaration of Competing Interest

None.

Acknowledgements

This work has been carried out as part of the Research Agreement between the Department of Civil and Mechanical Engineering (DICeM), University of Cassino and Southern Lazio, the Earth Science Department of the Sapienza University of Rome, and the Lazio region for the level 1 seismic microzonation of the Cassino municipality (OPCM n°3907/2010, DGR Lazio n°545/10). The open-access publication has been funded by the CERI Research Center on Geological Risks (CERI), Sapienza University of Rome. We thank Dr Antonella Paciello and Dr Vladimiro Verrubbi for the execution and processing of some of the microtremor measurements.

Appendix A. Supplementary data

Supplementary material related to this article can be found, in the online version, at doi:https://doi.org/10.1016/j.enggeo.2019.105333.

References

Albano, M., Lancia, M., Saroli, M., Modoni, G., Mugnozza, G.S., Croce, P., 2015. Seismic Microzonation of the Cassino Plain, in: Engineering Geology for Society and Territory - Volume 5. Springer International Publishing, Cham, pp. 1115–1118. https://doi.org/10.1007/978-3-319-09048-1_212.

Allin Cornell, C., 1968. Engineering seismic risk analysis. Bull. Seismol. Soc. Am. 58, 1583–1606.

Amadei, G., Bernabini, M., Maino, A., Orlando, L., 1978. Studio gravimetrico della bassa valle dei fiumi Sacco e Liri (Italia centrale). Boll. del Serv. Geol. d'Italia XCIX 19–28.

Amato, A., Azzara, R., Chiarabba, C., Cimini, G.B., Cocco, M., Di Bona, M., Margheriti, L., Mazza, S., Mele, F., Selvaggi, G., Basili, A., Boschi, E., Courboulex, F., Deschamps, A., Gaffet, S., Bittarelli, G., Chiaraluce, L., Piccinini, D., Ripepe, M., 1998. The 1997 Umbria-Marche, Italy, Earthquake Sequence: A first look at the main shocks and aftershocks. Geophys. Res. Lett. 25, 2861–2864. https://doi.org/10.1029/98GL51842.

Aucelli, P.P.C., Di Paola, G., Valente, E., Amato, V., Bracone, V., Cesarano, M., Di Capua, G., Scorpio, V., Capalbo, A., Pappone, G., Ravera, F., Rosskopf, C.M., 2018. First assessment of the local seismic amplification susceptibility of the isernia province (Molise region, southern italy) by the integration of geological and geomorphological studies related to the first level seismic microzonation project. Environ. Earth Sci. 77. https://doi.org/10.1007/s12665-018-7319-4.

Barchi, M.R., Galadini, F., Lavecchia, G., Messina, P., Michetti, A.M., Peruzza, L., Pizzi, A., Tondi, E., Vittori, E., 2000. Sintesi delle Conoscenze Sulle Faglie Attive in Italia Centrale: Parametrizzazione ai Fini della Caratterizzazione della Pericolosità Sismica. Monografie GNDT - Gruppo Nazionale per La Difesa Dai Terremoti, Roma.

Bard, P.-Y., 1999. Microtremor measurements: a tool for site effect estimation? In: Second International Symposium on the Effects of Surface Geology on Seismic Motion. AA Balkema, Rotterdam. pp. 1251–1279.

Bard, P.-Y., 1985. The two dimensional resonance of sediment-filled valleys. Bull. Seismol. Soc. Am. 75, 519–541.

Bard, P.-Y., Bouchon, M., 1980. The seismic response of sediment-filled valleys. Part 1. The case of incident SH waves. Bull. Seismol. Soc. Am. 70, 1263–1286.

Beneo, E., 1942. Le zone strutturali e le possibilità petrolifere dellaValle Latina (Lazio).

Boll. del Reg. Uff. Geol. d'Italia 67, 1–5.
Bernard, P., Zollo, A., 1989. The Irpinia (Italy) 1980 earthquake: detailed analysis of a complex normal faulting. J. Geophys. Res. 94, 1631. https://doi.org/10.1029/JB094iB02p01631.
Bielak, J., Xu, J., Ghattas, O., 1999. Earthquake ground motion and structural response in Alluvial Valleys. J. Geotech. Geoenviron. Eng. 125, 413–423. https://doi.org/10.1061/(ASCE)1090-0241(1999)125:5(413).
Bignardi, S., 2017. The uncertainty of estimating the thickness of soft sediments with the HVSR method: a computational point of view on weak lateral variations. J. Appl. Geophys. 145, 28–38. https://doi.org/10.1016/j.jappgeo.2017.07.017.
Boncio, P., Amoroso, S., Vessia, G., Francescone, M., Nardone, M., Monaco, P., Famiani, D., Di Naccio, D., Mercuri, A., Manuel, M.R., Galadini, F., Milana, G., 2018. Evaluation of liquefaction potential in an intermountain Quaternary lacustrine basin (Fucino basin, central Italy). Bull. Earthq. Eng. 16, 91–111. https://doi.org/10.1007/s10518-017-0201-z.
Boni, C., 2003. Le risorse idriche sotterranee e sorgive della conca di Cassino. Ann. di Ig. Med. Prev. e di Comunità 15 (Suppl. 1), 53–56.
Boni, C., Bono, P., Di FIlippo, M., Martelli, M.G., Toro, B., 1982. Carta del tetto del potenziale serbatoio (Lazio sud-occidentale). Contributo Alla Conoscenza Delle Potenzialità Geotermiche Della Toscana e Del Lazio. CNR-PFE-RF 15, Roma.
Boni, C.F., Bono, P., Capelli, G., 1986. Schema idrogeologico dell'Italia centrale. Mem. della Soc. Geol. Ital. 35, 991–1012.
Borges, J.F., Silva, H.G., Torres, R.J.G., Caldeira, B., Bezzeghoud, M., Furtado, J.A., Carvalho, J., 2016. Inversion of ambient seismic noise HVSR to evaluate velocity and structural models of the Lower Tagus Basin, Portugal. J. Seismol. 20, 875–887. https://doi.org/10.1007/s10950-016-9564-x.
Bosi, V., 1995. Evidenze di attivita` tettonica durante il pleistocene medio-olocene nel Lazio sud-orientale ed aree attigue. Pubblicazioni Istituto Nazionale Di Geofisica, Roma, pp. 1–32.
Cara, F., Di Giulio, G., Cavinato, G.P., Famiani, D., Milana, G., 2011. Seismic characterization and monitoring of Fucino Basin (Central Italy). Bull. Earthq. Eng. 9, 1961–1985. https://doi.org/10.1007/s10518-011-9282-2.
Cavinato, G.P., Sirna, M., 1988. Elementi di tettonica transpressiva lungo la linea di Atina (Lazio meridionale). Mem. della Soc. Geol. Ital. 41, 1179–1190.
Celico, P., Stanganelli, V., 1978. Indagini geoelettriche per la definizione di alcuni nodi strutturali dell'Appennino carbonatico centro-meridionale.
Centamore, E., Di Manna, P., Rossi, D., 2007. Kinematic evolution of the Volsci Range: a new overview. Boll. della Soc. Geol. Ital. 126, 159–172.
Cipollari, P., Cosentino, D., 1999. Cronostratigrafia dei depositi neogenici del settore ernico-simbruino, Appennino centrale. Boll. della Soc. Geol. Ital. 118, 439–459.
Cipollari, P., Cosentino, D., 1995. Miocene unconformities in the Central Apennines: geodynamic significance and sedimentary basin evolution. Tectonophysics 252, 375–389. https://doi.org/10.1016/0040-1951(95)00088-7.
Civico, R., Sapia, V., Di Giulio, G., Villani, F., Pucci, S., Baccheschi, P., Amoroso, S., Cantore, L., Di Naccio, D., Hailemikael, S., Smedile, A., Vassallo, M., Marchetti, M., Pantosti, D., 2017. Geometry and evolution of a fault-controlled Quaternary basin by means of TDEM and single-station ambient vibration surveys: the example of the 2009 L'Aquila earthquake area, central Italy. J. Geophys. Res. Solid Earth 122, 2236–2259. https://doi.org/10.1002/2016JB013451.
D'Amico, V., Picozzi, M., Baliva, F., Albarello, D., 2008. Ambient noise measurements for preliminary site-effects characterization in the Urban area of Florence, Italy. Bull. Seismol. Soc. Am. 98, 1373–1388. https://doi.org/10.1785/0120070231.
Del Monaco, F., Tallini, M., De Rose, C., Durante, F., 2013. HVNSR survey in historical downtown L'Aquila (central Italy): site resonance properties vs. Subsoil model. Eng. Geol. 158, 34–47. https://doi.org/10.1016/j.enggeo.2013.03.008.
Devoto, G., 1965. Lacustrine pleistocene in the lower Liri valley. Geol. Rom. 4, 291–368.
DISS Working Group, 2018. Database of Individual Seismogenic Sources (DISS), Version 3.2.1: a Compilation of Potential Sources for Earthquakes Larger Than M 5.5 in Italy and Surrounding Areas. https://doi.org/10.6092/INGV.IT-DISS3.2.1.
Ewald, M., Igel, H., Hinzen, K.G., Scherbaum, F., 2006. Basin-related effects on ground motion for earthquake scenarios in the Lower Rhine Embayment. Geophys. J. Int. 166, 197–212. https://doi.org/10.1111/j.1365-246X.2006.02909.x.
Galadini, F., Falcucci, E., Galli, P., Giaccio, B., Gori, S., Messina, P., Moro, M., Saroli, M., Scardia, G., Sposato, A., 2012. Time intervals to assess active and capable faults for engineering practices in Italy. Eng. Geol. 139–140, 50–65. https://doi.org/10.1016/j.enggeo.2012.03.012.
Galadini, F., Meletti, C., Vittori, E., 2000. Stato delle conoscenze sulle faglie attive in Italia: elementi geologici di superficie. Le Ricerche Del GNDT Nel Campo Della Pericolosità Sismica (1996–1999). CNR-Gruppo Nazionale per La Difesa Dai Terremoti, Rome, pp. 107–136.
Galli, P., Castenetto, S., Peronace, E., 2017. The macroseismic intensity distribution of the 30 October 2016 earthquake in central Italy (m w 6.6): seismotectonic implications. Tectonics 36, 2179–2191. https://doi.org/10.1002/2017TC004583.
Galli, P., Castenetto, S., Peronace, E., 2012. The MCS macroseismic survey of the Emilia 2012 earthquakes. Ann. Geophys. 55. https://doi.org/10.4401/ag-6163.
Galli, P.A.C., Naso, J.A., 2009. Unmasking the 1349 earthquake source (southern Italy): paleoseismological and archaeoseismological indications from the Aquae Iuliae fault. J. Struct. Geol. 31, 128–149. https://doi.org/10.1016/j.jsg.2008.09.007.
Gallipoli, M.R., Mucciarelli, M., Castro, R.R., Monachesi, G., Contri, P., 2004. Structure, soil-structure response and effects of damage based on observations of horizontal-to-vertical spectral ratios of microtremors. Soil Dyn. Earthq. Eng. 24, 487–495. https://doi.org/10.1016/j.soildyn.2003.11.009.
Gorstein, M., Ezersky, M., 2015. Combination of HVSR and MASW methods to obtain shear wave velocity model of subsurface in Israel. Int. J. Geohazard. Environ. 1, 20–41. https://doi.org/10.15273/ijge.2015.01.004.
Gosar, A., Lenart, A., 2010. Mapping the thickness of sediments in the Ljubljana Moor basin (Slovenia) using microtremors. Bull. Earthq. Eng. 8, 501–518. https://doi.org/10.1007/s10518-009-9115-8.
Gosar, A., Rošer, J., Šket Motnikar, B., Zupančič, P., 2010. Microtremor study of site effects and soil-structure resonance in the city of Ljubljana (central Slovenia). Bull. Earthq. Eng. 8, 571–592. https://doi.org/10.1007/s10518-009-9113-x.
Hudson, G., Wackernagel, H., 1994. Mapping temperature using kriging with external drift: theory and an example from scotland. Int. J. Climatol. 14, 77–91. https://doi.org/10.1002/joc.3370140107.
Iannucci, R., Martino, S., Paciello, A., D'Amico, S., Galea, P., 2018. Engineering geological zonation of a complex landslide system through seismic ambient noise measurements at the Selmun Promontory (Malta). Geophys. J. Int. 213, 1146–1161. https://doi.org/10.1093/gji/ggy025.
Ibs-von Seht, M., Wohlenberg, J., 1999. Microtremor measurements used to map thickness of Soft sediments. Bull. Seismol. Soc. Am. 89, 250–259.
Isaaks, E.H., Srivastava, R.M., 1989. An Introduction to Applied Geostatistics. Oxford Univ. Press, New York. An Introd. to Appl. geostatistics. Oxford Univ. Press, New York.
Knapmeyer-Endrun, B., Golombek, M.P., Ohrnberger, M., 2016. Rayleigh wave ellipticity modeling and inversion for shallow structure at the proposed InSight landing site in Elysium Planitia, Mars. Space Sci. Rev 1–44. https://doi.org/10.1007/s11214-016-0300-1.
Konno, K., Ohmachi, T., 1988. Ground-motion characteristics estimated from spectral ratio between horizontal and vertical components of microtremor. Bull. Seismol. Soc. Am. 88, 228–241.
Kramer, S.L., 1996. Geotechnical Earthquake Engineering. Prentice-Hall, Inc.https://doi.org/10.1007/978-3-540-35783-4.
Krige, D.G., 1966. Two-dimensional weighted moving average trend surfaces for ore-evaluation. J. South African Inst. Min. Metall. 66, 13–38.
Krige, D.G., 1951. A statistical approach to some mine valuation and allied problems on the Witwatersrand. J. South. African Inst. Min. Metall. 52, 119–139.
Matheron, G., 1963. Principles of geostatistics. Econ. Geol. 58, 1246–1266. https://doi.org/10.2113/gsecongeo.58.8.1246.
Meletti, C., Montaldo, V., 2007. . Stime di pericolosità sismica per diverse probabilità di superamento in 50 anni: valori di ag.
Milana, G., Cultrera, G., Bordoni, P., Bucci, A., Cara, F., Cogliano, R., Di Giulio, G., Di Naccio, D., Famiani, D., Fodarella, A., Mercuri, A., Pischiutta, M., Pucillo, S., Riccio, G., Vassallo, M., 2019. Local site effects estimation at Amatrice (Central Italy) through seismological methods. Bull. Earthq. Eng. 1–27. https://doi.org/10.1007/s10518-019-00587-3.
MIT, 2018. Aggiornamento delle "Norme tecniche per le costruzioni.". Gazz. Uff. 42.
Modoni, G., Darini, G., Spacagna, R.L., Saroli, M., Russo, G., Croce, P., 2013. Spatial analysis of land subsidence induced by groundwater withdrawal. Eng. Geol. 167, 59–71. https://doi.org/10.1016/j.enggeo.2013.10.014.
Molnar, S., Cassidy, J.F., Castellaro, S., Cornou, C., Crow, H., Hunter, J.A., Matsushima, S., Sánchez-Sesma, F.J., Yong, A., 2018. Application of microtremor horizontal-to-Vertical spectral ratio (MHVSR) analysis for site characterization: state of the art. Surv. Geophys. 39, 613–631. https://doi.org/10.1007/s10712-018-9464-4.
Nakamura, Y., 1989. A method for dynamic characteristics estimation of subsurface using microtremor on the ground surface. Q. Rep. Railw. Tech. Reasearch Inst. 30, 25–33.
Nguyen, F., Van Rompaey, G., Teerlynck, H., Van Camp, M., Jongmans, D., Camelbeeck, T., 2004. Use of microtremor measurement for assessing site effects in Northern Belgium – interpretation of the observed intensity during the M S = 5.0 June 11 1938 earthquake. J. Seismol. 8, 41–56. https://doi.org/10.1023/B:JOSE.0000009498.84531.71.
Novarese, V., 1926. La Valle Latina. Mem. Descr. della Cart. Geol. di Ital. XX.
Oliver, M.A., Webster, R., 2014. A tutorial guide to geostatistics: computing and modelling variograms and kriging. Catena 113, 56–69. https://doi.org/10.1016/j.catena.2013.09.006.
Oubaiche, E.H., Chatelain, J., Hellel, M., Wathelet, M., Machane, D., Bensalem, R., Bouguern, A., 2016. The relationship between ambient vibration H/V and SH transfer function: some experimental results. Seismol. Res. Lett. 87, 1112–1119. https://doi.org/10.1785/0220160113.
Pagliaroli, A., Avalle, A., Falcucci, E., Gori, S., Galadini, F., 2015. Numerical and experimental evaluation of site effects at ridges characterized by complex geological setting. Bull. Earthq. Eng. 13, 2841–2865. https://doi.org/10.1007/s10518-015-9753-y.
Paolucci, R., Evangelista, L., Mazzieri, I., Schiappapietra, E., 2016. The 3D numerical simulation of near-source ground motion during the Marsica earthquake, central Italy, 100 years later. Soil Dyn. Earthq. Eng. 91, 39–52. https://doi.org/10.1016/j.soildyn.2016.09.023.
Parolai, S., Bormann, P., Milkereit, C., 2002. New relationships between Vs, thickness of sediments, and resonance frequency calculated by the H/V ratio of seismic noise for the cologne area (Germany). Bull. Seismol. Soc. Am. 92, 2521–2527. https://doi.org/10.1785/0120010248.
Pasquali, V., Castorina, F., Cipollari, P., Cosentino, D., Lo Mastro, S., 2007. I depositi tardo-orogenici della Valle Latina meridionale: stratigrafia e implicazioni cinematiche per l'evoluzione dell'Appennino centrale. Boll. della Soc. Geol. Ital. 126, 101–118.
Pebesma, E.J., 2004. Multivariable geostatistics in S: the gstat package. Comput. Geosci. 30, 683–691. https://doi.org/10.1016/j.cageo.2004.03.012.
Polcari, M., Albano, M., Saroli, M., Tolomei, C., Lancia, M., Moro, M., Stramondo, S., 2014. Subsidence Detected by Multi-Pass Differential SAR Interferometry in the Cassino Plain (Central Italy): Joint Effect of Geological and Anthropogenic Factors? Remote Sens. 6, 9676–9690. https://doi.org/10.3390/rs6109676.
QGIS Development Team, 2018. QGIS Geographic Information System ver.3.0.1.
R Core Team, 2018. R: A Language and Environment for Statistical Computing.

Roberts, G.P., Michetti, A.M., 2004. Spatial and temporal variations in growth rates along active normal fault systems: an example from the Lazio–abruzzo Apennines, central Italy. J. Struct. Geol. 26, 339–376. https://doi.org/10.1016/S0191-8141(03)00103-2.

Roberts, G.P., Michetti, A.M., Cowie, P., Morewood, N.C., Papanikolaou, I., 2002. Fault slip-rate variations during crustal-scale strain localisation, central Italy. Geophys. Res. Lett. 29https://doi.org/10.1029/2001GL013529. 9-1-9–4.

Rosa-Cintas, S., Clavero, D., Delgado, J., López-Casado, C., Galiana-Merino, J.J., Garrido, J., 2017. Characterization of the shear wave velocity in the metropolitan area of Málaga (S Spain) using the H/V technique. Soil Dyn. Earthq. Eng. 92, 433–442. https://doi.org/10.1016/j.soildyn.2016.10.016.

Rovida, A., Locati, M., Camassi, R., Lolli, B., Gasperini, P. (Eds.), 2016. CPTI15, the 2015 Version of the Parametric Catalogue of Italian Earthquakes. https://doi.org/10.6092/INGV.IT-CPTI15.

Şafak, E., 2001. Local site effects and dynamic soil behavior. Soil Dyn. Earthq. Eng. 21, 453–458. https://doi.org/10.1016/S0267-7261(01)00021-5.

Salameh, C., Bard, P.-Y., Guillier, B., Harb, J., Cornou, C., Gérard, J., Almakari, M., 2017. Using ambient vibration measurements for risk assessment at an urban scale: from numerical proof of concept to Beirut case study (Lebanon). Earth Planets Space 69, 60. https://doi.org/10.1186/s40623-017-0641-3.

Saroli, M., Lancia, M., Albano, M., Modoni, G., Moro, M., Scarascia Mugnozza, G., 2014. New geological data on the Cassino intermontane basin, central Apennines, Italy. Rend. Lincei 25, 189–196. https://doi.org/10.1007/s12210-014-0338-5.

Saroli, M., Lancia, M., Petitta, M., 2019. The geology and hydrogeology of the Cassino plain (central Apennines, Italy): redefining the regional groundwater balance. Hydrogeol. J. 1–17. https://doi.org/10.1007/s10040-019-01953-w.

Saroli, M., Moro, M., 2012. San Pietro Infine Basin. Field–trip guidebook, in: AIGeo (Ed.). In: 16th Joint Geomorphological Meeting. Rome.

SESAME, 2004. Guidelines for the implementation of the H/V spectral ratio technique on ambient vibrations: measurements, processing, and interpretation. SESAME Eur. Res. Proj. WP12 – Deliv. D23.12. .

Tarabusi, G., Caputo, R., 2016. The use of HVSR measurements for investigating buried tectonic structures: the Mirandola anticline, Northern Italy, as a case study. Int. J. Earth Sci. 1–13. https://doi.org/10.1007/s00531-016-1322-3.

Trevisani, S., Boaga, J., 2018. Passive seismic prospecting in Venice historical center for impedance contrast mapping. Environ. Earth Sci. 77, 733. https://doi.org/10.1007/s12665-018-7918-0.

Trevisani, S., Boaga, J., Agostini, L., Galgaro, A., 2017. Insights into bedrock surface morphology using low-cost passive seismic surveys and integrated geostatistical analysis. Sci. Total Environ. 578, 186–202. https://doi.org/10.1016/j.scitotenv.2016.11.041.

Vessia, G., Russo, S., 2013. Relevant features of the valley seismic response: the case study of Tuscan Northern Apennine sector. Bull. Earthq. Eng. 11, 1633–1660. https://doi.org/10.1007/s10518-013-9456-1.

Wells, D.L., Coppersmith, K.J., 1994. New empirical relationships among magnitude, rupture length, rupture width, rupture area, and surface displacement. Bull. Seismol. Soc. Am. 84, 974–1002.